MARTIN MARIETTA ENERGY SYSTEMS LIBRARIES
3 4456 0364506 3

ORNL-3261
UC-80 – Reactor Technology
TID-4500 (17th ed.)

NUCLEAR ANALYSES OF THE N.S. SAVANNAH REACTOR WITH ZIRCALOY OR STAINLESS STEEL AS FUEL-ELEMENT CONTAINERS

E. E. Gross
B. W. Colston
M. L. Winton

CENTRAL RESEARCH LIBRARY
DOCUMENT COLLECTION
LIBRARY LOAN COPY
DO NOT TRANSFER TO ANOTHER PERSON
If you wish someone else to see this document, send in name with document and the library will arrange a loan.

OAK RIDGE NATIONAL LABORATORY
operated by
UNION CARBIDE CORPORATION
for the
U.S. ATOMIC ENERGY COMMISSION

Printed in USA. Price $1.75 Available from the

Office of Technical Services
U. S. Department of Commerce
Washington 25, D. C.

LEGAL NOTICE

This report was prepared as an account of Government sponsored work. Neither the United States, nor the Commission, nor any person acting on behalf of the Commission:

A. Makes any warranty or representation, express or implied, with respect to the accuracy, completeness, or usefulness of the information contained in this report, or that the use of any information, apparatus, method, or process disclosed in this report may not infringe privately owned rights; or

B. Assumes any liabilities with respect to the use of, or for damages resulting from the use of any information, apparatus, method, or process disclosed in this report.

As used in the above, "person acting on behalf of the Commission" includes any employee or contractor of the Commission to the extent that such employee or contractor prepares, handles or distributes, or provides access to, any information pursuant to his employment or contract with the Commission.

ORNL-3261

UC-80 – Reactor Technology
TID-4500 (17th ed.)

Contract No. W-7405-eng-26

Reactor Division

NUCLEAR ANALYSES OF THE N.S. SAVANNAH REACTOR WITH ZIRCALOY OR STAINLESS STEEL AS FUEL-ELEMENT CONTAINERS

E. E. Gross B. W. Colston
M. L. Winton

Date Issued

APR 24 1962

OAK RIDGE NATIONAL LABORATORY
Oak Ridge, Tennessee
operated by
UNION CARBIDE CORPORATION
for the
U. S. ATOMIC ENERGY COMMISSION

MARTIN MARIETTA ENERGY SYSTEMS LIBRARIES

3 4456 0364506 3

CONTENTS

Page

Abstract v

1. Introduction 1

2. Description of the Core 3

3. Analytical Model 5

Four-Group Model 5

Thermal Group 11

Nonthermal Groups 13

Geometrical Model 21

Fuel-Pin Cells 21

Slab Fuel-Element Can Cell and Control Rod Boundary Conditions 23

Two-Dimensional Fuel-Element Can Cell 29

Two-Dimensional Full-Core Geometry 30

4. Comparison with Critical Experiment Data 31

5. Results for Core I Fuel Elements in Stainless Steel Fuel-Element Containers 34

Four-Group Cross Sections 34

Fuel-Pin-Cell Results 36

Slab Fuel-Element Can-Cell Results 38

Two-Dimensional Fuel-Element Can-Cell Results 43

Two-Dimensional Full-Core Results 44

6. Comparison of Zircaloy and Stainless Steel as Fuel-Container Materials for Core I Fuel Elements 49

Comparison of Static Multiplication Factors at 68°F 49

Comparison of Static Multiplication Factors at Full Power 51

Comparison of Power Distribution 52

7. Reactivity Lifetime Comparison of Cores with Zircaloy or Stainless Steel Fuel Containers 53

References 58

Appendices

Apendix 1. Core Material Compositions 63

Appendix 2. Multigroup Cross Sections 65

ABSTRACT

Nuclear comparisons were made of Zircaloy and stainless steel as fuel-element container (or "egg-crate") materials in the N.S. SAVANNAH core I design. In order to make the comparison, a four-group model employing a combination of one-dimensional S_n transport-theory and two-dimensional diffusion-theory calculations was devised. The main features of the analytical model are geometrical detail and the use of the S_n method to obtain transport-theory equivalent-boundary conditions at the surface of control rods.

Application of the four-group model to the N.S. SAVANNAH core I design revealed that, relative to stainless steel fuel-element containers, a Zircaloy fuel-element container structure would increase control rod worth by $\Delta k = 0.043$ and would increase core reactivity by $\Delta k = 0.062$ for the same fuel enrichment. Although these two fuel-element container materials produced slightly different power distributions, the over-all peak-to-average power ratio appeared to be the same.

In order to complete the comparison, simple one-dimensional radial burnup calculations were performed. The burnup calculations indicated that the heterogeneous effect of the fuel-element containers on control rod worth would allow a 60% increase in the reactivity lifetime of core I-type fuel elements in Zircaloy fuel-element containers relative to the reactivity lifetime attainable in stainless steel fuel-element containers.

NUCLEAR ANALYSES OF THE N.S. SAVANNAH REACTOR WITH ZIRCALOY OR STAINLESS STEEL AS FUEL-ELEMENT CONTAINERS

E. E. Gross B. W. Colston
M. L. Winton

1. INTRODUCTION

As a part of the program for upgrading the N.S. SAVANNAH power plant, ways to improve core performance and fuel cycle economics are being investigated. In this program, emphasis has been placed on evaluating improvements in core I that can be effected by relatively minor design changes rather than by considering a new core design.

One such improvement appears to be offered by the replacement of stainless steel core components by components fabricated of a structural material with a much lower thermal-neutron absorption cross section, such as Zircaloy. The substitution of Zircaloy for stainless steel in core I would permit a reduction in U^{235} fuel inventory for a given reactivity lifetime, but this saving would be somewhat offset by the relatively high material and fabrication costs of Zircaloy. The choice of Zircaloy or stainless steel as a core structural material is, therefore, not always clear-cut and should be evaluated on the basis of a specific design.

Most of the stainless steel in core I is present either in the fuel elements in the form of tubing or in the fuel-element container grid structure (the so-called "egg crate") in the form of essentially flat plates. Replacement of steel by Zircaloy in the egg crate appears more attractive than in the fuel tubes for the following reasons:

1. The relatively long life of the egg crate (several core loadings) permits the cost of the Zircaloy to be amortized over a long period.

2. Because of the proximity of the egg crate to the control rods, substitution of Zircaloy for stainless steel in this region should increase control-rod worth. This effect has been demonstrated for an aluminum egg crate in the N.S. SAVANNAH critical experiments.[1]

3. Being adjacent to a water gap, the egg crate is in a higher thermal-flux region than the fuel tubes. Thus, a substitution of Zircaloy

for a given amount of stainless steel in the egg-crate region can result in a greater saving of fuel than the same substitution in the fuel-tube region.

4. Fabrication of a Zircaloy egg crate should be relatively simple compared with the fabrication of a fuel bundle composed of many Zircaloy fuel tubes.

Items 2 and 3 depend upon the details of the core design, and such detail is usually ignored in general studies comparing Zircaloy and stainless steel as reactor materials.[2,3] In contrast to a general study, the present investigation is an attempt to evaluate the effects of material substitution for a particular core design, with due regard for the heterogeneous nature of the design. The core I designs[4] for the fuel element, control rod, and control-rod followers, therefore, form the basis for comparing egg-crate materials in this study.

Determination of the detailed characteristics of a heterogeneous water-moderated reactor requires the solution of the Boltzman transport equation for the neutron flux as a function of position, direction, and energy over the whole range of these variables. Disregarding the matter of cost, not only is such a solution beyond the capabilities of present computers, but the present state of cross-section information would make the computation difficult to justify. Thus, although the theory of neutron transport and slowing down is well understood, rigorous application of the theory in most cases is a practical impossibility, and many compromises both in the physics and in the mathematics must be made to obtain results. These compromises, together with cross-section uncertainties, make reactor physics calculations rather suspect, and the usual practice of including critical experimentation as part of the design procedure is a manifestation of the unreliability of reactor calculations. Even when critical-experiment data have been obtained, there have been many cases (although not documented) of error in extrapolation to the prototype design.

The evaluations reported herein may be considered in the nature of an extrapolation from the core I design for which there are available critical-experiment data,[1] as well as zero-power experiment data,[5] on the prototype core. As we shall see, however, the seemingly minor exchange

of stainless steel for Zircaloy in the N.S. SAVANNAH core I egg crate produces profound changes in the core properties, and the preceding comments on the present reliability of reactor calculations is intended to give proper perspective to the calculated results. Despite encouraging agreement between the calculations reported herein and certain pertinent experimental data, the perturbing effect of the Zircaloy egg crate on core I properties is of such a magnitude that further experimentation would be required before the advantages of a Zircaloy egg crate could be fully exploited. The calculations described in this report could, however, provide useful guidance in executing such a design change.

Although the analytical methods used in this study were developed for a particular reactor design, it is believed that the general approach, especially with regard to treatment of control rods, may have wider interest and application. Therefore, following a description of the core design, the physical and geometrical models employed in the analysis are described in some detail. Results obtained by using these models are then compared with experimental data, and calculated results comparing stainless steel and Zircaloy egg crates are presented. Finally, simple one-dimensional burnup calculations complete the comparison of stainless steel and Zircaloy egg crates for N.S. SAVANNAH core I.

2. DESCRIPTION OF THE CORE

Core I is a heterogeneous, low-enrichment, water-moderated and water-reflected reactor designed and built by The Babcock & Wilcox Company. Although details of the design may be found elsewhere,[4] a description of the core is presented here for completeness.

A view of the top of the core as it appeared during the zero power test[5] is shown in Fig. 1. The core configuration is defined by a 6-by-6 square array of stainless steel fuel boxes on a 9.73-in. pitch with the corner boxes missing; there are 32 fuel boxes in all. The boxes serve to provide channels for the 21 cruciform control rods and control-rod followers as well as to direct the coolant flow in this two-pass core. The outer 16 fuel boxes form one core pass (flow downward), and the inner 16

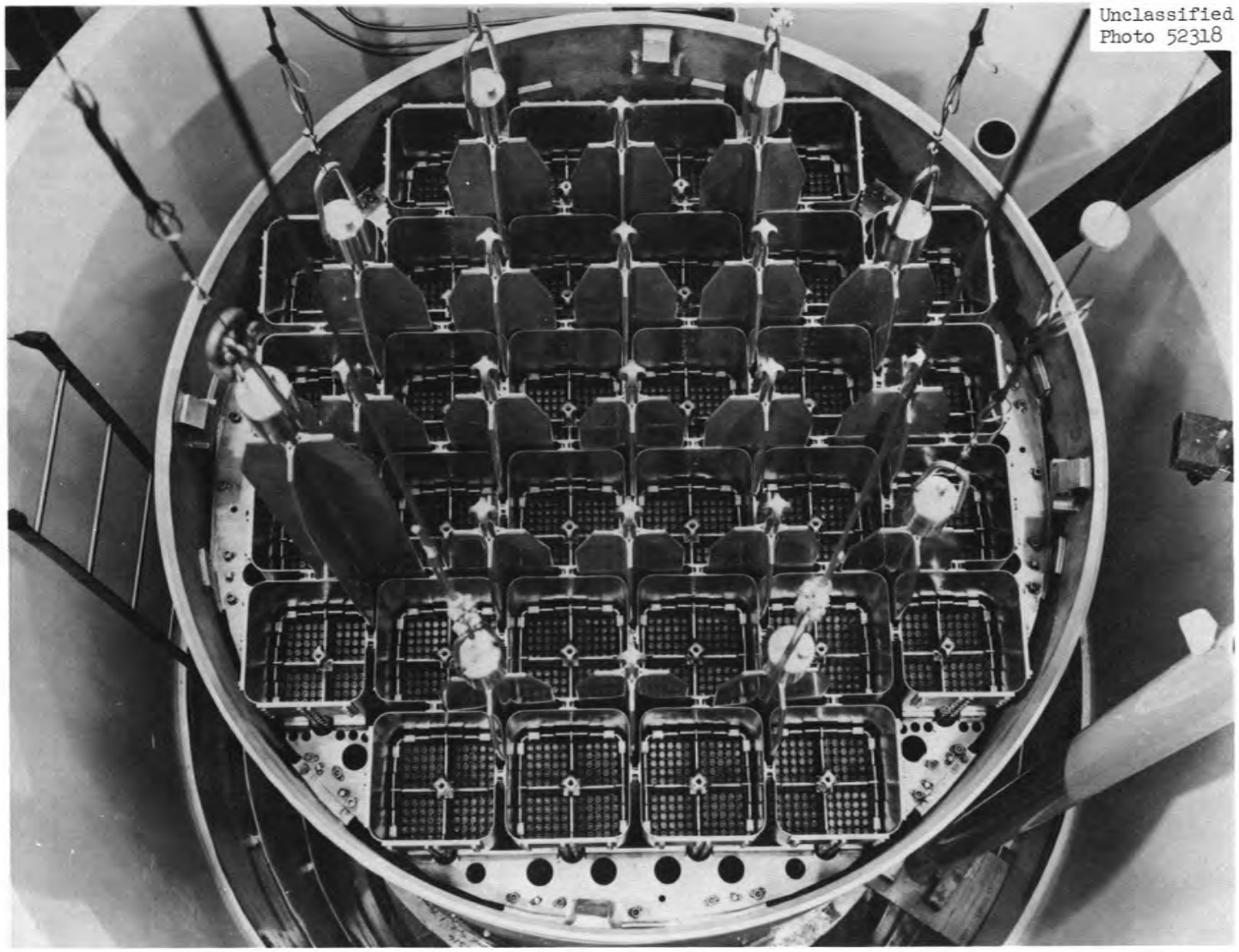

Fig. 1. Top View of N.S. SAVANNAH Core I.

fuel boxes comprise the second core pass (flow upward). The fuel boxes are held together in a rigid structure (the so-called "egg crate") by "H"-shaped stainless steel pieces called spacer bars which are riveted to adjacent fuel-element containers. A cutaway view of the fuel-element container assembly, or egg crate, is shown in Fig. 2. It is the substitution of Zircaloy for stainless steel as this egg crate material that is the subject of this study.

A fuel element consisting of a square array of 164 cylindrical fuel pins fits into each fuel box. A view of one of the approximately 6-ft-long (active height = 66.0 in.) fuel elements is shown in Fig. 3. The corner tubes, which would complete the 13-by-13 array, are omitted to reduce the local power peaking that occurs at the corners of fuel elements adjacent to a control-rod follower. Also, the central tube in each fuel bundle is hollow and serves both as a structural member and provides a means for reducing the core reactivity, if necessary, by the addition of boron-steel filler rods. The stainless steel fuel tubes are held together in a rigid bundle by 1-in.-long stainless steel ferrules brazed to the fuel rods every 8 in. axially along the fuel element.

Details of a section of the core through a ferrule plane are shown in Fig. 4. This figure clearly illustrates the very heterogeneous nature and the geometrical complexity of the N.S. SAVANNAH core. Mixed geometries abound; cylindrical fuel pins form a square array; and, although the almost square fuel-element containers form a square array, they have rounded corners. The control-rod follower, which is attached to the bottom of each control rod in order to reduce thermal-flux peaking between containers when a control rod is withdrawn, is also complex in geometry and composition. Such complexities are common features of most practical power reactor designs.

3. ANALYTICAL MODEL

Four-Group Model

A desire to account for the two-dimensional aspects of the N.S. SAVANNAH core design led to the use of the PDQ code,[6] which is a two-

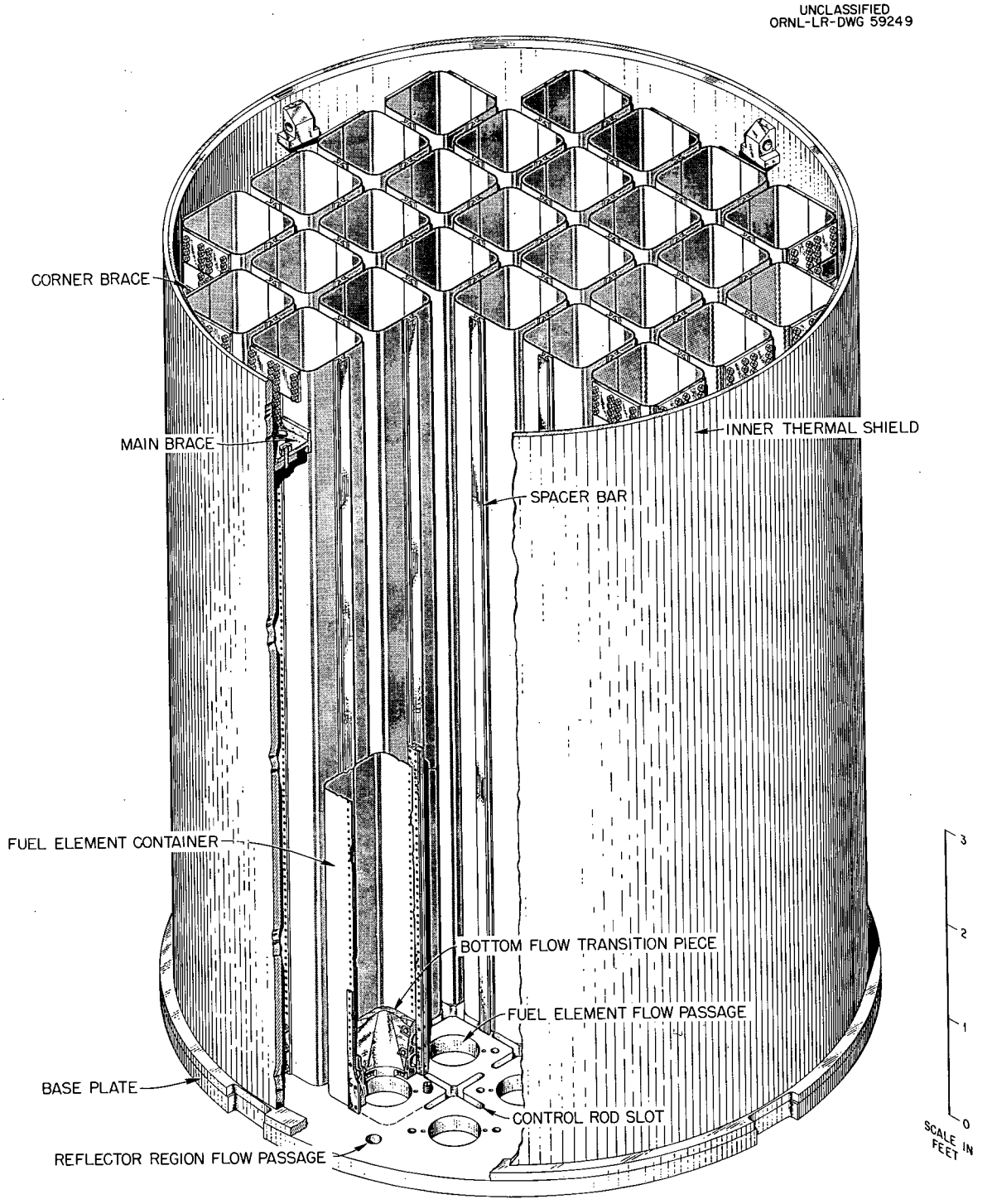

Fig. 2. N.S. SAVANNAH Fuel Element Container Assembly.

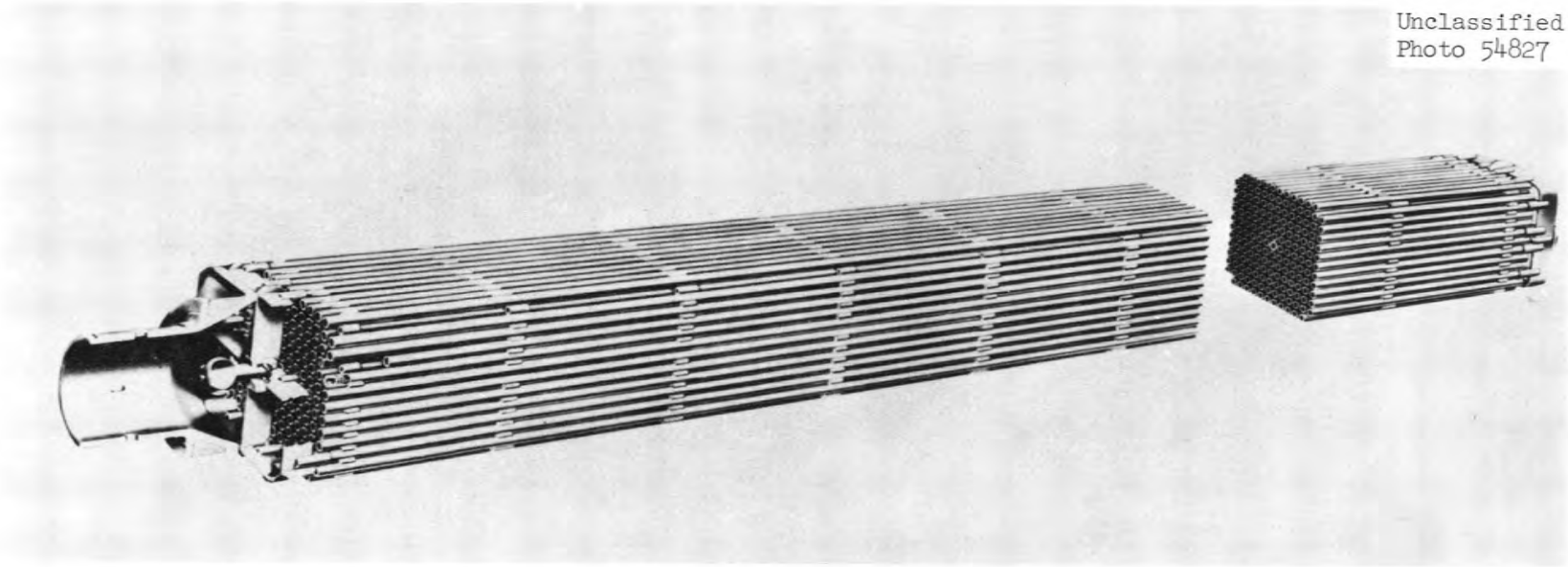

Fig. 3. N.S. SAVANNAH Core I Fuel Element.

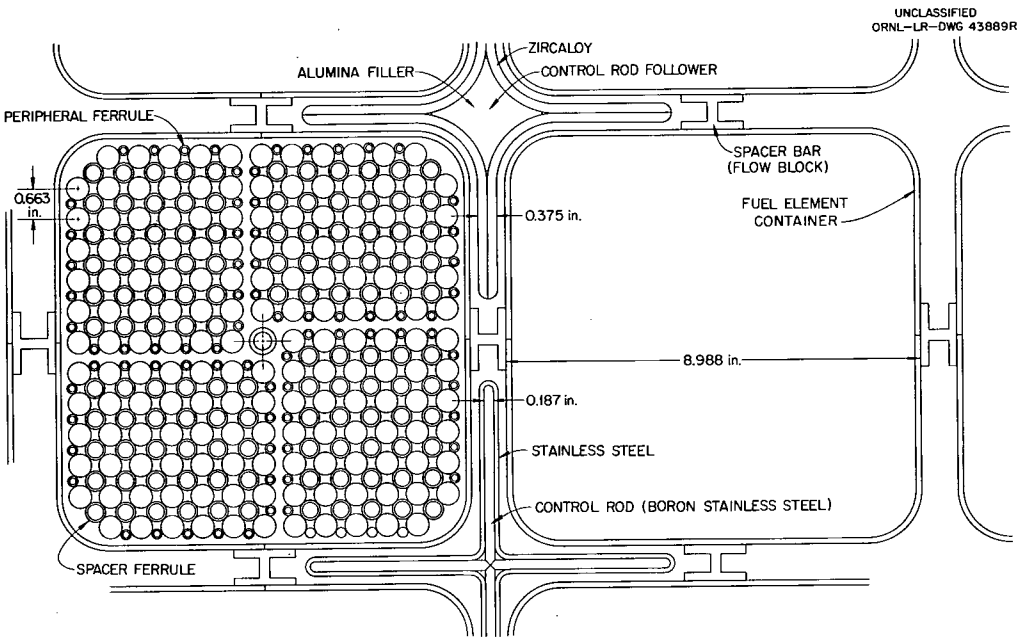

Fig. 4. N.S. SAVANNAH Core I Details: Section Through a Ferrule Plane.

dimensional diffusion-theory code limited to four or less energy groups. The full four-group capabilities of the code were utilized to handle the strong absorption properties of the core I control rods.

Strongly absorbing regions, such as control rods, can be represented in the PDQ code by a current per unit flux boundary condition at the surface of the absorbing region. To obtain realistic transport-theory values for the control rod boundary conditions, the one-dimensional SNG transport-theory code[7,8] was employed. The SNG code also served to obtain reaction rates throughout the strongly absorbing UO_2 fuel region where, again, diffusion theory was not expected to apply. The resulting analytical model was thus a combination of one-dimensional transport-theory and two-dimensional diffusion-theory codes.

The four-group conservation equations solved by the SNG code are

$$\underline{\Omega}\cdot\underline{\nabla}\phi_1(\underline{r},\underline{\Omega}) + (\Sigma_{a1} + \Sigma_{tr1} + \Sigma_{12} + \Sigma_{13} + \Sigma_{14})\phi_1(\underline{r},\underline{\Omega})$$

$$= \frac{\nu_c}{4\pi}\left[\Sigma_{f1}\phi_1(\underline{r}) + \Sigma_{f2}\phi_2(\underline{r}) + \Sigma_{f3}\phi_3(\underline{r}) + \Sigma_{f4}\phi_4(\underline{r})\right] + \frac{\Sigma_{tr1}}{4\pi}\phi_1(\underline{r}) \quad , \quad \text{(1a)}$$

$$\underline{\Omega}\cdot\underline{\nabla}\phi_2(\underline{r},\underline{\Omega}) + (\Sigma_{a2} + \Sigma_{tr2} + \Sigma_{23} + \Sigma_{24})\phi_2(\underline{r},\underline{\Omega})$$

$$= \frac{\Sigma_{12}}{4\pi}\phi_1(\underline{r}) + \frac{\Sigma_{tr2}}{4\pi}\phi_2(\underline{r}) \quad , \qquad (1b)$$

$$\underline{\Omega}\cdot\underline{\nabla}\phi_3(\underline{r},\underline{\Omega}) + (\Sigma_{a3} + \Sigma_{tr3} + \Sigma_{34})\phi_3(\underline{r},\underline{\Omega})$$

$$= \frac{\Sigma_{13}}{4\pi}\phi_1(\underline{r}) + \frac{\Sigma_{23}}{4\pi}\phi_2(\underline{r}) + \frac{\Sigma_{tr3}}{4\pi}\phi_3(\underline{r}) \quad , \qquad (1c)$$

$$\underline{\Omega}\cdot\underline{\nabla}\phi_4(\underline{r},\underline{\Omega}) + (\Sigma_{a4} + \Sigma_{tr4})\phi_4(\underline{r},\underline{\Omega})$$

$$= \frac{\Sigma_{14}}{4\pi}\phi_1(\underline{r}) + \frac{\Sigma_{24}}{4\pi}\phi_2(\underline{r}) + \frac{\Sigma_{34}}{4\pi}\phi_3(\underline{r}) + \frac{\Sigma_{tr4}}{4\pi}\phi_4(\underline{r}) \quad , \qquad (1d)$$

where Σ_{ag} is the absorption cross section in group g (that is, group 1, 2, 3, or 4), Σ_{trg} is the transport scattering cross section in group g, Σ_{fg} is the fission cross section in group g, $\Sigma_{gg'}$ is the cross section for transfer from group g to group g′, and υ_c is the eigenvalue. The total flux in group g, $\phi_g(\underline{r})$, is related to the flux per unit solid angle, $\phi_g(\underline{r},\underline{\Omega})$, by

$$\phi_g(\underline{r}) = \int_{4\pi} \phi_g(\underline{r},\underline{\Omega})\, d\Omega \quad . \qquad (2)$$

It should be noted that fissions can occur in any group, but the resulting fission neutrons are all born with energies in group 1.

As presently constituted, the SNG code is limited to isotropic scattering and isotropic transfer. Consequently, the in-group scattering term, $\Sigma_{trg}\phi_g(\underline{r})$, cancels on both sides of Eq. 1 upon integration over Ω. The value of the in-group scattering cross section therefore plays no essential role in Eq. 1 with respect to the over-all neutron balance, and the use of the transport scattering cross section for this term provides continuity between the transport-theory calculations and the diffusion-theory calculations.

The four-group conservation equations solved by the PDQ diffusion-theory code are

$$-\frac{1}{3\Sigma_{tr1}}\nabla^2\phi_1(\underline{r}) + (\Sigma_{a1} + \Sigma'_{12})\phi_1(\underline{r})$$

$$= \upsilon_c[\Sigma_{f1}\phi_1(\underline{r}) + \Sigma_{f2}\phi_2(\underline{r}) + \Sigma_{f3}\phi_3(\underline{r}) + \Sigma_{f4}\phi_4(\underline{r})] \quad , \tag{3a}$$

$$-\frac{1}{3\Sigma_{tr2}}\nabla^2\phi_2(\underline{r}) + (\Sigma_{a2} + \Sigma'_{23})\phi_2(\underline{r}) = \Sigma'_{12}\phi_1(\underline{r}) \quad , \tag{3b}$$

$$-\frac{1}{3\Sigma_{tr3}}\nabla^2\phi_3(\underline{r}) + (\Sigma_{a3} + \Sigma'_{34})\phi_3(\underline{r}) = \Sigma'_{23}\phi_2(\underline{r}) \quad , \tag{3c}$$

$$-\frac{1}{3\Sigma_{tr4}}\nabla^2\phi_4(\underline{r}) + \Sigma_{a4}\phi_4(\underline{r}) = \Sigma'_{34}\phi_3(\underline{r}) \quad , \tag{3d}$$

where all the cross sections have the same values as in Eq. 1, except that the transfer cross sections are related by

$$\Sigma'_{g,g+1} = \sum_{g'=1}^{g} \Sigma_{g',g+1} \quad . \tag{4}$$

That is, the PDQ code is limited to transfer from one group to the group immediately below. This is not a serious limitation for the four groups used in this study, even for hydrogen scattering, since scattering from one group to the group below accounts for 99% of the total transfers.

All group cross sections in Eqs. 1 and 3 are flux-averaged values according to

$$\sigma^m_{gi} = \frac{\int_{E_g}^{E_{g-1}} \phi(E)\sigma^m_i(E)\, dE}{\int_{E_g}^{E_{g-1}} \phi(E)\, dE} \quad , \tag{5}$$

where σ^m_{gi} is the average microscopic cross section over the energy range $E_g \leq E \leq E_{g-1}$ for type i neutron reactions in energy group g with material m. The flux per unit energy, $\phi(E)$, is related to the total flux in group g, ϕ_g, by

$$\phi_g = \int_{E_g}^{E_{g-1}} \phi(E)\, dE \quad . \tag{6}$$

The energy dependence of the flux necessary to evaluate the integrals in Eq. 5, together with the treatment of cross-section data, are presented below.

Thermal Group

Thermal Flux Energy Distribution. It has been customary to assume a Maxwellian distribution for the thermal flux of the form

$$\phi(E) \sim E\, e^{-E/KT} \quad , \qquad 0 < E < E_c \quad , \tag{7}$$

where T is the absolute temperature of the moderator, K is the Boltzman gas constant, and E_c is the upper energy limit of the thermal group. This distribution arises if the neutrons are assumed to be in thermal equilibrium with the moderator atoms; however, the presence of absorption prevents the usual thermal equilibrium condition as well as the Maxwellian solution for the flux energy distribution. Although the solution for the flux energy distribution in the presence of arbitrary absorption cannot be written in analytical form, it has been solved for various cases by numerical methods.[9] For small macroscopic absorption cross sections, the thermal-neutron-flux energy distribution appears to have the Maxwellian shape (Eq. 7) shifted to a higher temperature. Apparent Maxwellian neutron temperatures for a variety of space-independent absorption problems have been obtained for light- and heavy-water moderators by Brown.[10] Thermal-neutron-flux hardening in the N.S. SAVANNAH core was partially accounted for by using a hardened neutron temperature based on the work

of Brown. For the ratio of the flux- and volume-weighted 2200-m/sec macroscopic absorption cross section to the flux- and volume-weighted epithermal slowing-down cross section of the N.S. SAVANNAH design (~0.19), the hardened neutron temperature corresponds to 0.0294 ev when the moderator temperature corresponds to 0.0253 ev.

Thermal Cross Sections. The flux-averaged microscopic cross sections shown in Table 1 were obtained by using Eq. 7 for the energy dependence of the thermal flux, a hardened neutron temperature corresponding to kT = 0.0294 ev (where T is the neutron temperature), a thermal-group cutoff of 0.15 ev, and available cross section data.[11]

Table 1. Hardened Thermal-Group Cross Sections at 68°F

Material	Microscopic Cross Section (barns)		
	σ_a	$\upsilon\sigma_f$	$\sigma_s(1 - \bar{\mu}_0)$
U^{235}	550.81	1140.1	14.96
U^{238}	2.261	0	8.28
Stainless steel	2.48	0	9.65
Hydrogen	0.271	0	30.03
Oxygen	0	0	4.025

In obtaining the values given in Table 1, the absorption cross sections of U^{238}, stainless steel, and hydrogen were assumed to vary as 1/v in the thermal energy range. The transport cross section, $\sigma_s(1 - \bar{\mu}_0)$, for hydrogen bound in water was also taken to have a 1/v behavior with a 2200 m/sec value of 37.14 barns.[12] When Zircaloy followers were present in the core, the water and followers in the channels were assumed to be in a well-moderated thermal-neutron-flux distribution characterized by a Maxwellian temperature corresponding to kT = 0.0253 ev. Well-moderated thermal cross sections for channel materials are shown in Table 2. The absorption cross section of Zircaloy in Table 2 contains allowances for impurities in reactor-grade Zircaloy (composition given in Appendix 1).

Table 2. Well-Moderated Thermal-Group Cross Sections at 68°F

Material	Microscopic Cross Section (barns)	
	σ_a	$\sigma_s(1 - \bar{\mu}_0)$
Hydrogen	0.293	32.93
Oxygen	0	4.025
Zircaloy	0.164	6.25
Aluminum	0.204	1.36

The dependence of the average thermal cross section upon the moderator temperature was based on the work of Petrie et al.[13] With this temperature dependence, the hardened cross sections at 68°F given in Table 1 can be transferred to the 508°F conditions shown in Table 3.

Table 3. Hardened Thermal-Group Cross Sections at 508°F

Material	Microscopic Cross Section (barns)		
	σ_a	$\nu\sigma_f$	$\sigma_s(1 - \bar{\mu}_0)$
U^{235}	395.8	816.0	14.96
U^{238}	1.66	0	8.28
Stainless steel	1.80	0	9.65
Hydrogen	0.199	0	21.71
Oxygen	0	0	4.025

Similarly, the well-moderated thermal-group cross sections at 68°F given in Table 2 become the values given in Table 4 at 508°F.

Nonthermal Groups

Group Structure. The energy distribution of the slowing-down was determined by a multigroup slowing-down calculation using the GNU diffusion-theory code.[14] In the slowing-down calculation the core was approximated by a right-circular cylinder with a radius to give the same

Table 4. Well-Moderated Thermal-Group Cross Sections at 508°F

Material	Microscopic Cross Section (barns)	
	σ_a	$\sigma_s(1 - \bar{\mu}_0)$
Hydrogen	0.211	24.03
Oxygen	0	4.025
Zirconium	0.120	6.25
Aluminum	0.149	1.36

area as 32 fuel-element can cells (a can cell being a square with boundaries halfway between fuel-element containers). Leakage in the axial direction was accounted for by specifying an axial buckling which was taken from critical-experiment[1] axial flux plots to be $B_z^2 = 0.000294\ cm^{-2}$. With regard to the slowing-down neutrons, the core composition was taken to be a homogenized mixture of the core materials, although spatial variations of the slowing-down flux were partially accounted for on a four-group basis, as explained later. A typical result for the lethargy [$u(E) = \ln 10^7/E$] dependence of the slowing-down flux near the center of the core is shown in Fig. 5. The shape of the flux versus lethargy curve is found to be quite space independent up to within about one mean free path of the core reflector (water) boundary; however, as will be seen later from the four-group fuel-pin cell results (p. 36), the assumption of separability is violated on the small-scale level. Thus the assumed homogeneity of the core to slowing-down neutrons is certainly an oversimplification, since the same lethargy dependence of the slowing-down flux (Fig. 5) cannot apply to UO_2, stainless steel, Zircaloy, and H_2O.

On the basis of the calculated lethargy dependence of the slowing-down flux, the slowing-down energy range was divided into three groups, as shown in Fig. 5. The group 1 flux has a very pronounced energy variation determined to a large extent by the fission energy spectrum and the energy dependence of the hydrogen scattering cross section. In addition,

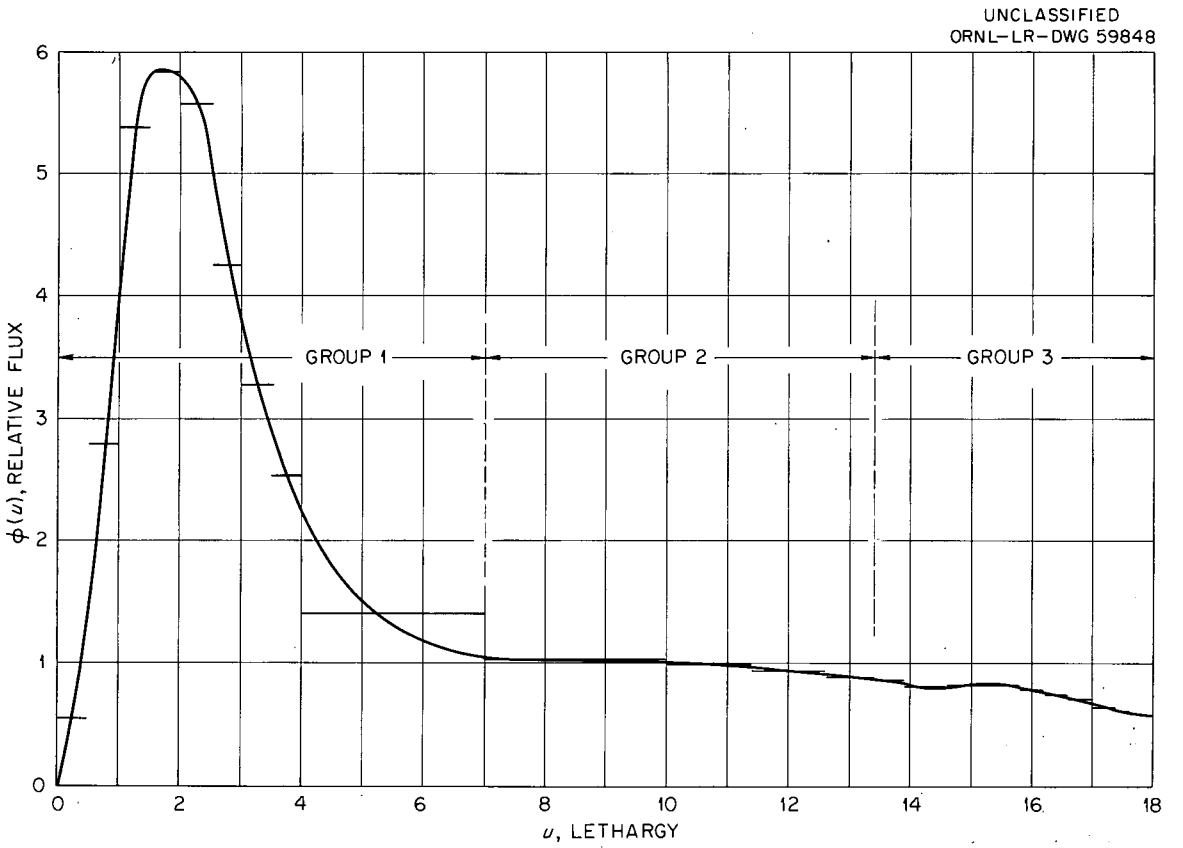

Fig. 5. Lethargy Distribution of Slowing-Down Flux for Core I at 68°F.

the group 1 flux shape is influenced by inelastic scattering and by fast-neutron leakage from the core.

The group 2 energy region is characterized by an almost 1/E energy dependence for the slowing-down flux. The energy dependence of the group 2 flux is a consequence of the following: (1) group 2 is below the fission source energy range, (2) the ratio of absorption to scattering is small, and (3) the hydrogen scattering cross section is independent of energy in this energy range.

The epithermal group flux, group 3, noticeably deviates from 1/E behavior, mainly because the absorption becomes increasingly important as the neutron energy decreases. The slow increase in the hydrogen scattering cross section also contributes to the deviation of the group 3 flux spectrum from 1/E behavior.

Many few-group methods assume all nonthermal groups to be characterized by 1/E energy dependence for the slowing-down flux, and this dependence is used to obtain flux-averaged group cross sections. The inadequacy of this energy dependence for reactors of the N.S. SAVANNAH type is manifest from Fig. 5. In addition, the slowing-down transfer cross section is usually defined as the ratio of a diffusion coefficient and an empirical age determined from measurements on infinite nonabsorbing media. The resulting nonthermal group cross sections obtained in this manner are then independent of core geometry and to a large extent insensitive to changes in core composition. In contrast to this practice, the method used here places complete reliance on the multigroup diffusion-theory determination of the slowing-down flux shown in Fig. 5. As discussed above, the shape of $\phi(u)$ is dependent on core geometry and core composition and is sensitive to changes in these parameters. Furthermore, changes in the shape of $\phi(u)$ are reflected as changes in the group cross sections (including transfer cross sections) through Eq. 5. The slowing-down model and the multigroup cross sections used to determine $\phi(u)$ thus contain the physics information with regard to our treatment of nonthermal neutron events.

Slowing-Down Model. In obtaining the energy distribution of the slowing-down flux, only "hydrogen-like" slowing down was considered. The contribution of inelastic scattering to the slowing-down process was accounted for by amending the hydrogen macroscopic scattering cross section at energy E, $\Sigma_s^H(E)$, to

$$\Sigma_s^{H'}(E) = \Sigma_s^H(E) + \sum_m \xi_{in}^m(E)\ \Sigma_{in}^m(E) \quad , \tag{8}$$

where $\xi_{in}^m(E)$ is the average logarithmic energy loss suffered by neutrons of energy E after an inelastic scattering collision with material m, and $\Sigma_{in}^m(E)$ is the macroscopic inelastic scattering cross section of material m for neutrons of energy E. This treatment of inelastic scattering is due to Perry.[15]

Justification for this treatment of inelastic scattering lies in the fact that the average fission-neutron energy is only slightly higher than the threshold energies for inelastic scattering in N.S. SAVANNAH core I materials. The low-lying excited energy levels are of the order of 1 Mev above the ground state for aluminum, zirconium, and the constituents of stainless steel and about 50 kev above the ground state of U^{238}. Thus, a fission neutron can lose a large fraction of its energy in an inelastic scattering collision, and a large energy loss is also a characteristic of neutron-proton scattering. Although the average neutron energy after an (n-p) collision is one-half the initial energy, inelastic neutron scattering collisions can produce much larger average neutron energy losses, and this effect is partially accounted for by the use of the logarithmic energy loss factor, $\xi_{in}(E)$. Values of $\xi_{in}(u)\ \sigma_{in}(u)$ based on available data[16–20] for U^{238}, stainless steel, zirconium, and aluminum for the first ten lethargy groups in GNU are shown in Table 5.

Table 5. "Hydrogen-Like" Microscopic Inelastic-Scattering Cross Sections

Group	Lethargy Limits	$\xi_{in}(u)\ \sigma_{in}(u)$ (barns)			
		U^{238}	Stainless Steel	Zirconium	Aluminum
1	0–0.5	0.852	2.434	3.35	0.90
2	0.5–1.0	0.852	0.925	2.73	0.80
3	1.0–1.5	0.852	0.523	1.96	0.650
4	1.5–2.0	0.852	0.473	0.77	0.100
5	2.0–2.5	0.852	0.271	0.20	0
6	2.5–3.0	0.852	0	0	0
7	3.0–3.5	0.852	0	0	0
8	3.5–4.0	0.852	0	0	0
9	4.0–7.0	0.852	0	0	0
10	7.0–10.0	0.852	0	0	0

Multigroup Cross Sections. Except for inelastic scattering cross sections, which are discussed and tabulated in the previous section, the multigroup cross sections used in all GNU determinations of the slowing-

down-flux lethargy distribution are tabulated in Appendix 2. This tabulation includes transport, absorption, and fission cross sections.

The transport cross sections used were those of an original GNU cross-section tape and appear to be in agreement with available data and other tabulations. The hydrogen and oxygen transport cross sections yield a Fermi age of about 30 cm^2 for fission neutrons in pure water, which is the usual result obtained from the diffusion approximation and hydrogen slowing down. Other than as a gross check on the transport cross sections of hydrogen and oxygen, the Fermi age plays no role in the present method. Rather than the usual definition of the transfer cross section as a ratio of a diffusion coefficient and a Fermi age, we determine the transfer cross section for hydrogen from group g to group g′, $\Sigma^H_{gg'}$, from the conservation of neutrons and the multigroup fluxes according to

$$\Sigma^H_{gg'} = \frac{e^{-U_{g'-1}} - e^{-U_{g'}}}{\sum_{i=I^o_g}^{I^f_g} \phi_i(u_i - u_{i-1})} \sum_{i=I^o_g}^{I^f_g} 3\Sigma^H_{tri}\, \phi_i(e^{u_i} - e^{u_{i-1}}) \quad , \tag{9}$$

where $I^f_{g'} - I^o_g$ is the number of groups in the multigroup calculation that makes up group g in the few-group model, U_g and U_{g-1} are the lethargy limits of group g, ϕ is the multigroup flux, and Σ^H_{tri} is the multigroup hydrogen transport cross section (equal to one-third the hydrogen scattering cross section). The terms in Eq. 9 are further clarified by Table 6. The exponential factors in Eq. 9 result from the hydrogen slowing-down model employed in the multigroup calculation. "Hydrogen-like" inelastic scattering transfer cross sections can be obtained in the same manner by the substitution of the $\xi^m_{in}\Sigma^m_{ini}$ from Eq. 8 for the $3\Sigma^H_{tri}$ in Eq. 9.

With the transformation of integrals to sums and proper definition of the transfer cross section, Eq. 9 may be recognized as an application of the definition given by Eq. 5 for a flux-averaged group cross section. The one exception to this definition is the group transport cross section, which, because of the diffusion approximation used in the slowing-down

Table 6. Relation Between Multigroup and Few-Group Quantities Appearing in Eq. 9

Multigroup Index (i)	Multigroup Lethargy Intervals ($u_{i-1} - u_i$)	Few-Group Index (g)	Few-Group Lethargy Intervals ($U_{g-1} - U_g$)	Multigroup Index Limits Corresponding to Group g (I_g)
1	0–0.5			$I_1^o = 1$
2	0.5–1.0			
3	1.0–1.5			
4	1.5–2.0			
5	2.0–2.5	1	0–7.0	
6	2.5–3.0			
7	3.0–3.5			
8	3.5–4.0			
9	4.0–7.0			$I_1^f = 9$
10	7.0–10.0			$I_2^o = 10$
11	10.0–11.4			
12	11.4–12.6	2	7.0–13.4	
13	12.6–13.4			$I_2^f = 13$
14	13.4–13.8			$I_3^o = 14$
15	13.8–14.6			
16	14.6–15.8			
17	15.8–16.2			
18	16.2–16.6	3	13.4–18.0	
19	16.6–17.0			
20	17.0–17.4			
21	17.4–17.6			
22	17.6–17.8			
23	17.8–18.0			$I_3^f = 23$
24	18.0–∞	4	18.0–∞	

calculation, must be averaged as the reciprocal of the transport cross section rather than as the transport cross section itself.

The multigroup absorption cross sections appearing in Appendix 2 were manufactured to agree with measured resonance-integral data,[21,22] using the energy behavior of the total cross section[11] as a guide. In the case of U^{235}, the total resonance-absorption integral was arbitrarily normalized to 1.5 times the resonance-fission integral.[21] The lack of knowledge concerning the ratio of the resonance-absorption integral to the resonance-fission integral for U^{235} is somewhat serious in cores of

the N.S. SAVANNAH type, since a 10% increase in this ratio (well within present uncertainty) would increase the calculated critical radius by about 10%. In the present study this uncertainty is not serious because we are comparing a core using stainless steel fuel containers with the same core using Zircaloy containers, and the same fuel cross section data are used throughout.

In obtaining multigroup absorption cross sections for U^{238}, the following empirical correlation based on the work of Hellstrand[22] on bulk UO_2 at 68°F was used:

$$I^{28} = 11.0 + 24.5 \frac{S}{M} \quad . \tag{10}$$

This correlation would give $I^{28} = 19.93$ barns for a single core I fuel pin ($S/M = 0.3645$ cm^2/g) in an infinite moderator. Applying a correction[23] to the surface-absorption term to take into account the presence of other fuel pins reduces the U^{238}-resonance integral of core I fuel pins in their lattice to $I^{28} = 18.85$ barns at room temperature (68°F).

For the temperature variation of the resonance integral of U^{238} in single fuel pins, the empirical correlation of Hellstrand et al.[24] was used

$$I^{28}(T) = I^{28}(T_0) \left[1 + \left(0.0058 + 0.005 \frac{S}{M}\right) (\sqrt{T} - \sqrt{T_0})\right] \quad , \tag{11}$$

where T is the absolute temperature of the UO_2 in °K and T_0 is any reference temperature in °K. To apply the lattice correction, the resonance integral must be expressable in terms of a volume plus a surface term (such as in Eq. 10), since the correction[23] is applied only to the surface term. To get the surface dependence of $I^{28}(T)$, we assumed that the temperature variation is a 50% surface effect and a 50% volume effect. The resulting U^{238} resonance integrals for single fuel pins and for fuel pins in the core I lattice are listed in Table 7 for room-temperature, zero-power, and full-power conditions. In Table 7, zero power corresponds to a uniform temperature of 508°F throughout the core. Full power corresponds to 508°F for the moderator and an importance-averaged fuel temperature

Table 7. U^{238}-Resonance Integral Data for Core I

Reactor Condition	I^{28} (barns)	
	Single Pin	Lattice
Room temperature (68°F)	19.93	18.85
Zero power, core at 508°F	20.85	19.21
Full power, moderator at 508°F, fuel at 1290°F	22.08	20.35

of 1290°F. The U^{238} multigroup cross sections listed in Appendix 2 have been manufactured to give the lattice resonance integrals in Table 7 using the total cross-section variation[11] as a guide.

Geometrical Model

The energy-averaged four-group cross sections obtained in the manner just described could be used to determine reaction rates throughout the N.S. SAVANNAH core. The geometry of this core, as illustrated by Fig. 4, is much too complicated, however, for determination of reaction rates in all core materials by a single calculation, and much simplification was required before gross flux distributions throughout a full-sized core could be computed. The simplification process employed was the usual one of successive homogenizations based on the symmetry properties of the core. By judicious use of available reactor codes, the present method of homogenization contains some novel combinations of one-dimensional transport-theory and two-dimensional diffusion-theory calculations, as discussed below.

Fuel-Pin Cells

The first step in simplification was to homogenize the fuel-pin region. It may be argued that the repetitive arrangement of fuel pins suggests defining a unit fuel-pin cell whose area is the square of the fuel-pin pitch. For an infinite array of fuel pins the net current across a

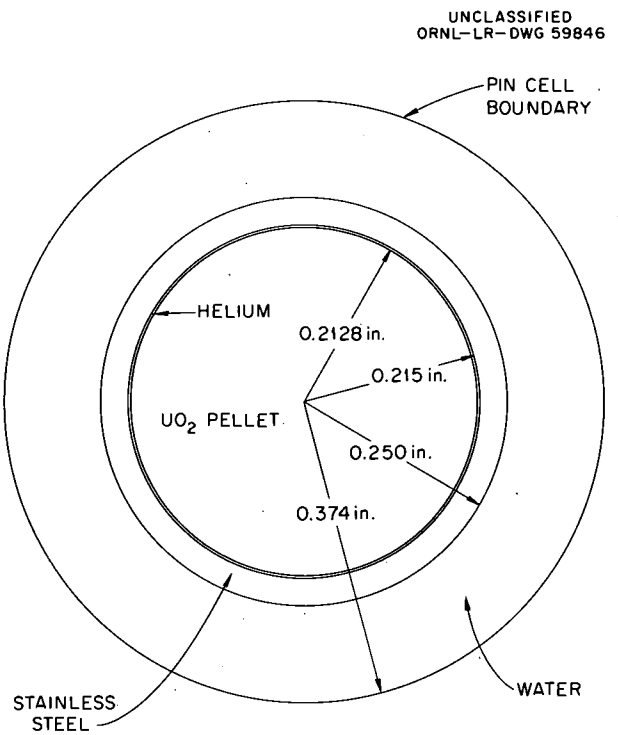

Fig. 6. Details of Geometrical Model Used for Fuel-Pin Cell of N.S. SAVANNAH Core I.

cell boundary should be zero, and a reasonable approximation for this boundary is the surface of a cylinder whose axis is coincident with the fuel-pin axis. The geometry of such a fuel-pin cell, with details of the UO_2 pellet, helium gap, and stainless steel dimensions for a core I fuel pin, is shown in Fig. 6. Information on the chemical composition of the pin-cell materials, as well as other core materials, is given in Appendix 1.

Zero-current boundary conditions on the pin-cell boundary and on the fuel-pin axis allow, in principle, determination of the flux distribution throughout the geometry of Fig. 6, provided the cross sections as functions of position, energy, and direction are known. Because there are severe cross-section changes over a distance comparable to the mean free path of a thermal neutron (~0.5 in.) and because the ratio of absorption to scattering is not small in the UO_2 and in the stainless steel cladding, a transport-theory solution for the pin-cell fluxes was obtained. This was accomplished by using the SNG code[7] to solve Eqs. 1 for the four-group fluxes and the eigenvalue υ_c. The solution to Eqs. 1 for the pin-cell geometry was carried out in both the so-called "S-4" and "S-8" approximations. This demonstrated that the S-4 approximation was quite adequate for a core I fuel-pin cell. The four-group fluxes so obtained were used for the computation of homogenized four-group cross sections representing the entire fuel-pin cell.

It should be pointed out that, throughout the stepwise homogenization procedure, Eqs. 1 or their diffusion-theory equivalents, Eqs. 3, were solved as coupled equations so that the flux in one energy group served as the source for neutrons in the lower energy groups. In this way, heterogeneous flux distributions at all energies were allowed for on a four-group basis (this also accounts for the omission of a fast-fission factor, ϵ, from Eqs. 1 and 3). In contrast, the usual practice is to homogenize only the thermal-group cross sections, with the assumption that the source flux (i.e., the epithermal flux) is spatially invariant. Although this assumption is a good one for a core I fuel-pin cell, it was found to be inadequate for the epithermal flux distribution throughout a fuel-element can cell, especially when control rods were present.

For that portion of the core containing stainless steel ferrules, the extra steel in the ferrules was represented by an additional annular steel region in a fuel-pin cell, as indicated in Fig. 7. The ferrule annulus was positioned midway in the water region surrounding a fuel pin and was assigned a thickness to give the known cross-sectional area of a ferrule. Again, the four-group equations (Eqs. 1) were solved for the four-group fluxes by using the SNG code and applying symmetry boundary conditions along the cell boundary and cell axis. As before, the resulting fluxes were used to obtain homogenized cross sections representing the ferrule region of the fuel.

The fuel-pin region containing ferrules was combined with the fuel-pin region not containing ferrules in the two-region slab geometry of Fig. 8. In obtaining Fig. 8, the repetitive arrangement of ferrule planes about every 8 in. axially in the core has been approximated by symmetry boundary conditions, as indicated by centerlines. The result of this calculation is homogenized cross sections representative of the entire fuel-pin region.

Slab Fuel-Element Can Cell and Control-Rod Boundary Conditions

Although homogenization of the fuel-pin region greatly reduced the complexity of the core geometry, there was still enough detail remaining that the full-core geometry could not be handled within the space-point

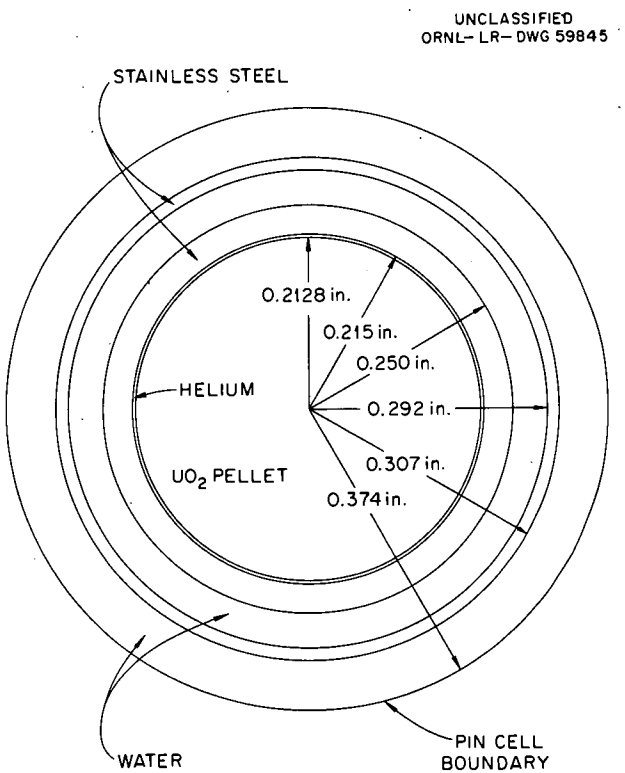

Fig. 7. Details of Geometrical Model Used for Fuel-Pin Cell with Ferrules, N.S. SAVANNAH Core I.

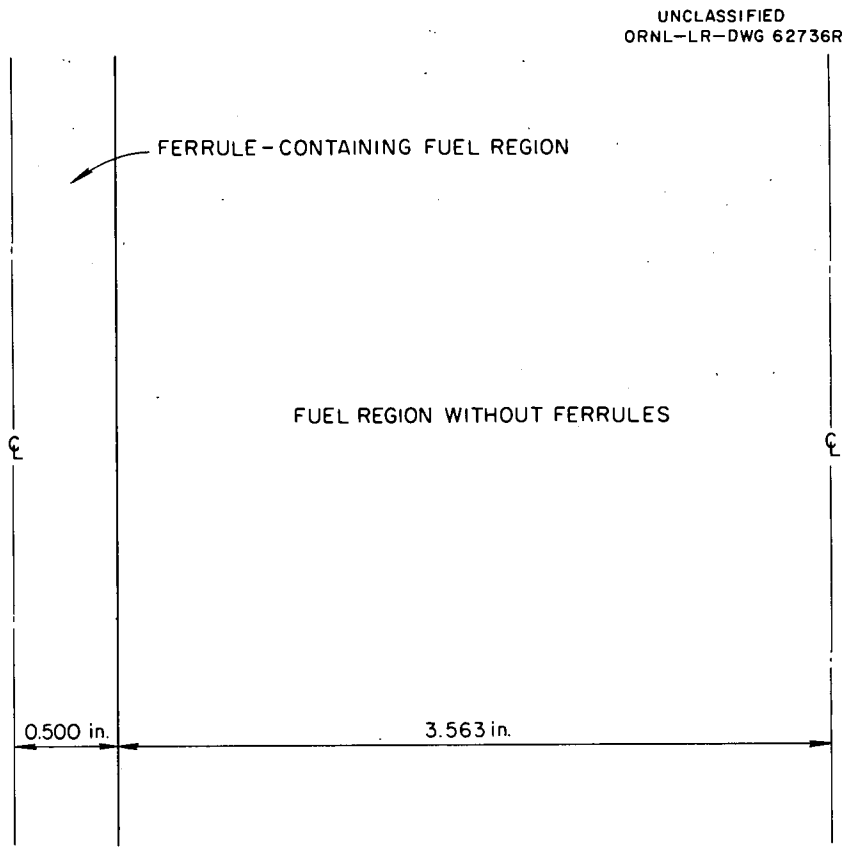

Fig. 8. Slab Geometry Model Used to Combine Ferrule-Containing Fuel-Pin Regions with Fuel-Pin Regions Not Containing Ferrules.

limitations of available two-dimensional diffusion-theory codes. The next step in simplification was therefore to further reduce the complexity of an individual fuel-element can cell, which is the next largest repetitive unit in the core. Before the two-dimensional aspects of a control rod could be treated, however, a technique for representing a strongly absorbing region suitable for diffusion theory was needed.

A satisfactory method of handling control rods within the limitations of diffusion theory is to specify the value of the current per unit flux at the boundary of the control-rod surface; i.e., specify the constant C_g to give

$$\left[\frac{\underline{n}\cdot\underline{J}_g(\underline{r})}{\phi_g(\underline{r})}\right]_S = -C_g \quad , \tag{12}$$

where $\underline{n}$ is a unit vector normal to the control-rod surface S, and $\underline{J}_g(\underline{r})$ is the neutron current density in group g at position $\underline{r}$. Using the diffusion theory approximation for the neutron current density

$$\underline{J} = \frac{-1}{3\Sigma_{tr}} \underline{\nabla}\phi \quad ,$$

the constant C_g may be related to the extrapolation distance δ_g by

$$\delta_g = \frac{1}{3\Sigma_{trg}C_g} \quad , \tag{13}$$

where Σ_{trg} is the transport scattering cross section in group g for the region immediately adjacent to the control rod.

For those energy groups in which the control rod is "black," it has been customary to use $C_g = 0.47$, which is the result from the classical transport-theory solution to the Milne problem.[25] For the nonblack or "gray" energy groups, it has been customary to apply diffusion theory to the control rods. The terms "black" and "gray" are, of course, quite vague. In addition, it is not clear that the Milne problem is at all

appropriate to multigroup problems involving a finite, heterogeneous geometry.

In the method used here, the usual uncertainty in the specification of control-rod boundary conditions is avoided by obtaining transport-theory results for C_g from an SNG solution of a suitable one-dimensional representation of a fuel-element can cell containing control rods. An appropriate one-dimensional core I can-cell geometry is shown in Fig. 9.

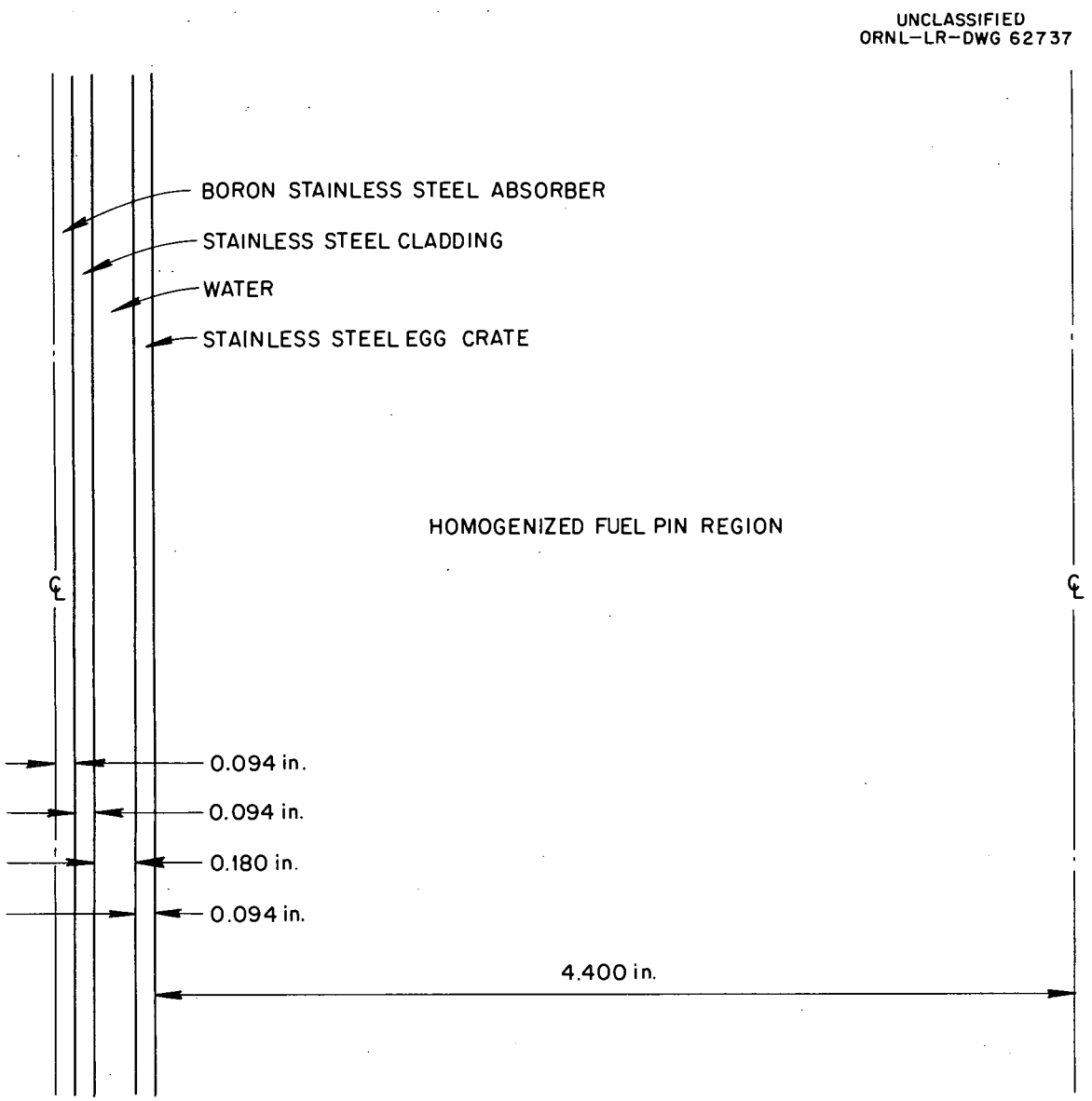

Fig. 9. Geometrical Model for Slab Can Cell with Control Rod.

An infinite array of such slab fuel elements and control rods would have zero-current boundary conditions along the centerlines shown in Fig. 9. The solution of Eqs. 1 for the geometry of Fig. 9 provides transport-theory values of C_g at the control rod surface that are representative of conditions a few mean free paths from the fuel-element corners and reflect the heterogeneous conditions in the immediate neighborhood of the control rod (e.g., the material constitution of the egg crate).

The SNG solutions for the slab geometry of Fig. 9 were obtained in the S-5 approximation with the discrete angles chosen so that $\mu = \cos\theta = \pm 0.1, \pm 0.5, \pm 1.0$. The adequacy of the S-5 approximation, as well as the capability of the S_n method in general, is well demonstrated by the solution to the Milne problem shown in Figs. 10 and 11. Figure 10 shows the

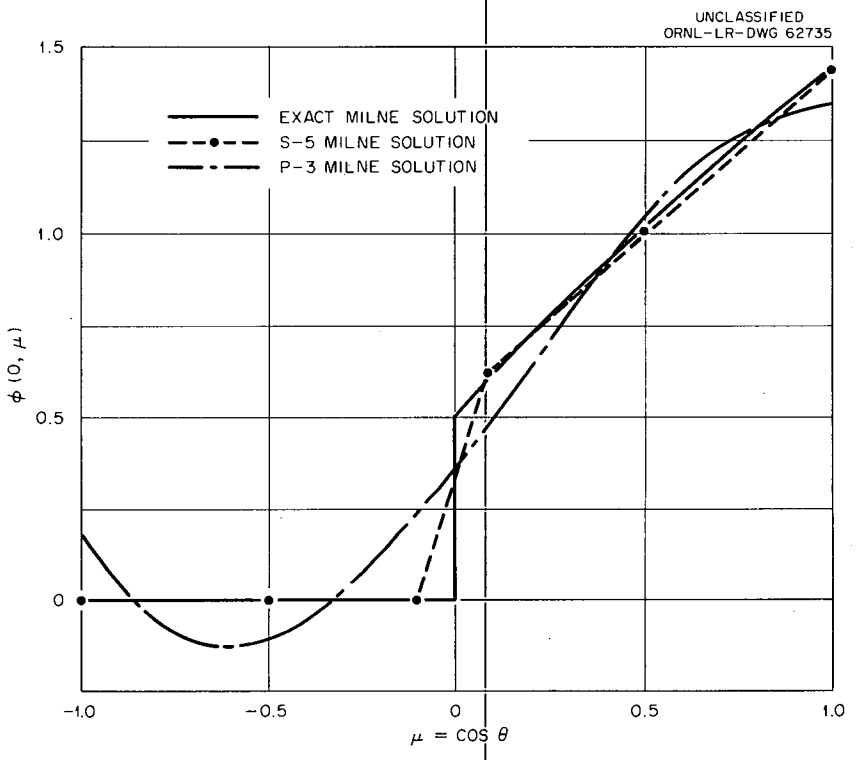

Fig. 10. Milne Problem Solutions for the Angular Flux at the Void Boundary Normalized so that $\int_{-1}^{+1} \phi(0,\mu)d\mu = 1$. Exact and P-3 solutions taken from ref. 25, p. 262.

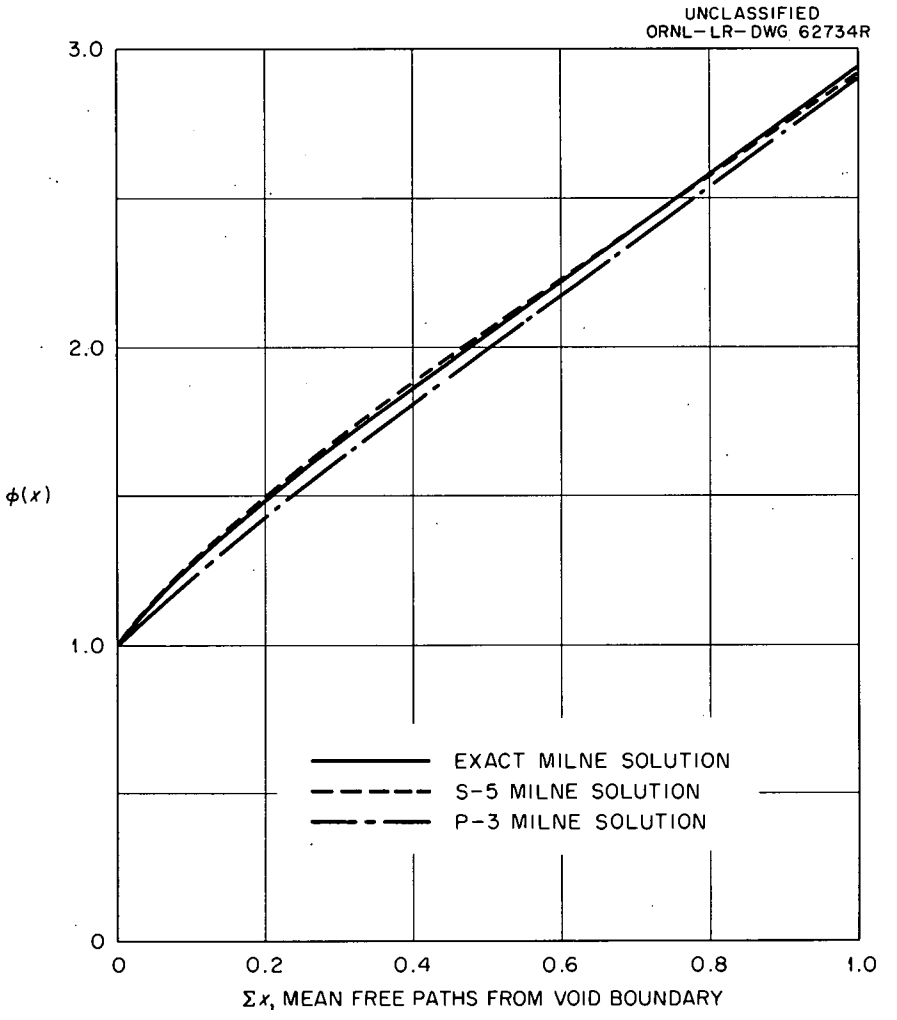

Fig. 11. Milne Problem Solutions for Total Flux Variation Near Void Boundary. Exact and P-3 solutions from ref. 25, p. 263.

angular distribution of monoenergetic neutrons at the boundary between a void and a semi-infinite diffusing region containing a plane isotropic source 20 mean free paths from the boundary. The SNG code solves Eqs. 1 for the discrete angles shown and assumes a linear variation of $\phi(\underline{r},\mu)$ with μ. Also shown in Fig. 10 are the exact and P-3 solutions[26] to the same problem. Figure 11 shows similar results for the variation of the total flux in the neighborhood of the void boundary. Again the S-5 solution compares favorably with the exact solution.

Two-Dimensional Fuel-Element Can Cell

The two-dimensional aspects of a fuel-element can cell were investigated in the geometry of Fig. 12 when followers were present and in the

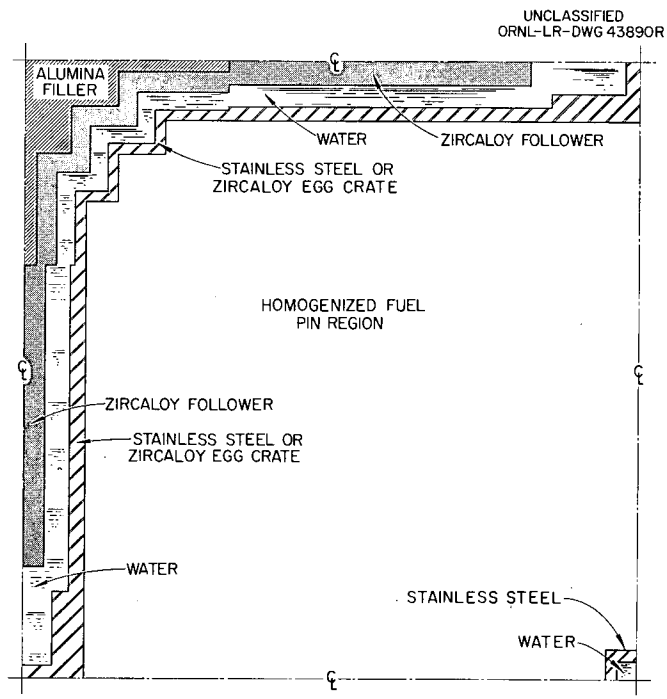

Fig. 12. Geometrical Model for One Quadrant of a Fuel-Element Can Cell with Followers.

geometry of Fig. 13 when control rods were present. The compromises in geometry necessary to perform a practical calculation are evident upon comparison of Figs. 12 and 13 with the actual core geometry shown in Fig. 4. In control-rod calculations based on Fig. 13, the control-rod region was replaced by a transport-theory boundary condition on the surface of the control rod obtained in the manner described previously. In generating this geometry, the nominal width of the water channel and the quantities of fuel container and follower materials were retained. The geometry for a Zircaloy fuel container was identical except that the width of the fuel container was increased in the fuel region by an amount (0.026 in.) dictated by preliminary stress analysis requirements.

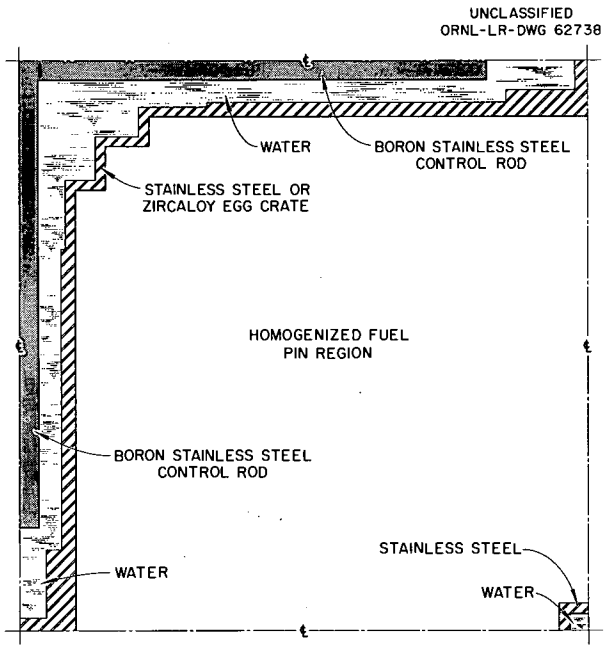

Fig. 13. Geometrical Model for One Quadrant of a Fuel-Element Can Cell with Control Rods.

A suitable simplification of the fuel-element can-cell geometry was found to be homogenization of the fuel-pin region with the central stainless steel support tube and the water filling this tube, homogenization of the egg-crate material with the channel water, and homogenization of the Zircaloy follower and its alumina filler. Multiplication factors obtained by using the simplified can-cell geometry were found to be only about 0.001 Δk greater than the multiplication factor obtained using the detailed geometry.

One fuel-element detail lacking in Figs. 12 and 13 is a thin (~0.3-cm-wide) water region between the homogenized fuel-pin region and the egg-crate region. This water region was accounted for by homogenizing it with the fuel-pin region (along with the central support tube and the water in this tube) and assuming the water region to be exposed to the same average fluxes as the egg crate. In this manner, account could be taken of variations in the thickness of this excess water region resulting from variations in thickness of the egg crate.

Two-Dimensional Full-Core Geometry

With these simplifications in the fuel-element can-cell geometry, the full-sized core was then represented by the geometry of Fig. 14. Again, when control rods were present in region 4, current per unit flux boundary conditions were used on the control-rod surface.

The leakage of neutrons in the axial direction was accounted for on a first-approximation basis by the use of a group-independent axial buckling based on measured axial-flux distributions.[1] The results from a

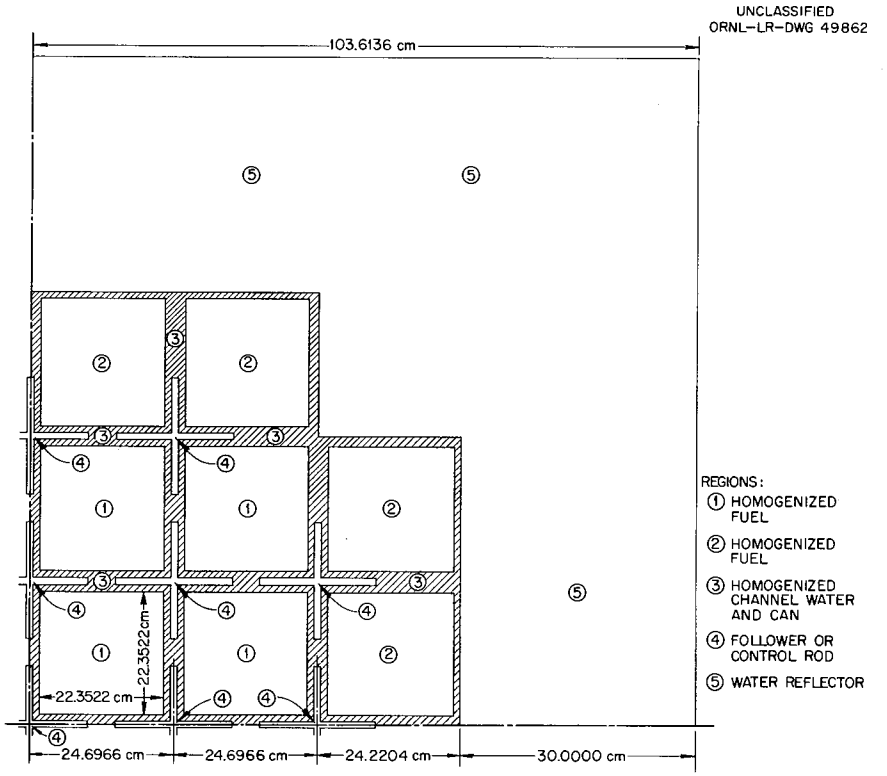

Fig. 14. Geometrical Model for One Quadrant of N.S. SAVANNAH Core I.

calculation in the geometry of Fig. 14 were used to homogenize the entire core, and a calculation of the full-sized core in r-z geometry was then performed. In this way, leakage from all surfaces of the core was treated explicitly.

4. COMPARISON WITH CRITICAL EXPERIMENT DATA

The experimental data most pertinent to an evaluation of fuel-element container materials are the data from the so-called "Marty II" and "Marty III" critical experiments.[1] These experiments compared the critical water heights of a stainless steel egg-crate core (Marty II) with an aluminum egg-crate core (Marty III) for a variety of control-rod patterns.

The Marty II and Marty III critical assemblies were composed of only 16 fuel elements rather than the 32 fuel elements contained in the prototype core. Details of a portion of Marty II are shown in Fig. 15.

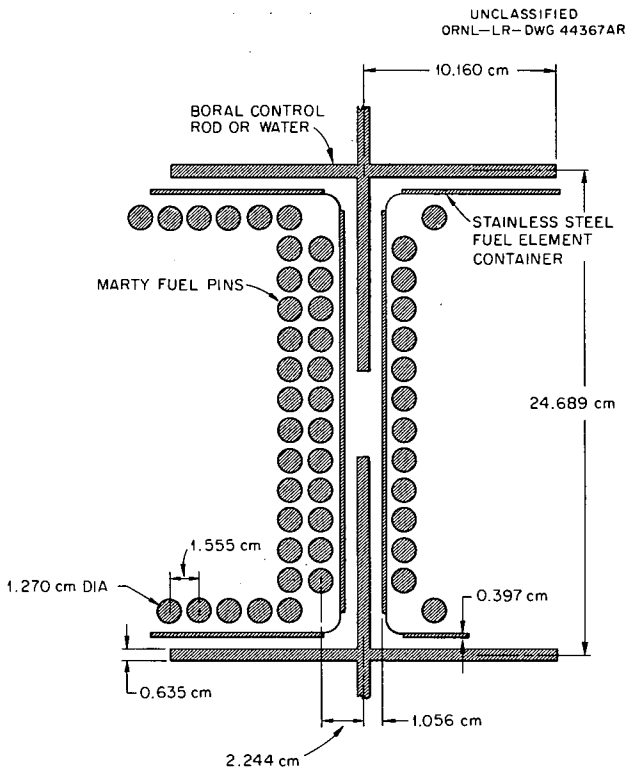

Fig. 15. Portion of Marty II Core.

Marty III is identical to Marty II except that the fuel-can material is 0.330-cm-thick aluminum.

These cores are considerably simpler than the prototype core (Fig. 4) in that they do not have ferrules, flow blocks, followers, or rounded egg-crate corners. This simplicity allows the full core to be represented in the geometry of Fig. 16, where the fuel-pin region has been homogenized by a fuel-pin cell calculation. In Fig. 16, a retracted control rod is replaced by water, as was the case in the experiment. It should be noted that the missing corner pins in each fuel element are accounted for by extending the channel water region into the fuel-pin region.

Using the four-group method outlined in the previous section, the static multiplication factors for certain rod configurations were calculated for Marty II and Marty III cores. Calculated results are compared with experimental results in Fig. 17. The experimental multiplication factors, k_d, i.e., the "dynamic" multiplication factors, were obtained from the reported excess reactivity values[1] by use of the equation

$$k_d = \frac{1}{1 - \rho\beta} , \qquad (14)$$

where ρ is the excess reactivity in dollars, and β is the delayed neutron yield per fission neutron and is taken to be 0.00706. The errors quoted for the experimental values in Fig. 17 are based only on reproducibility of critical water height positions.

UNCLASSIFIED
ORNL-LR-DWG 52969AR

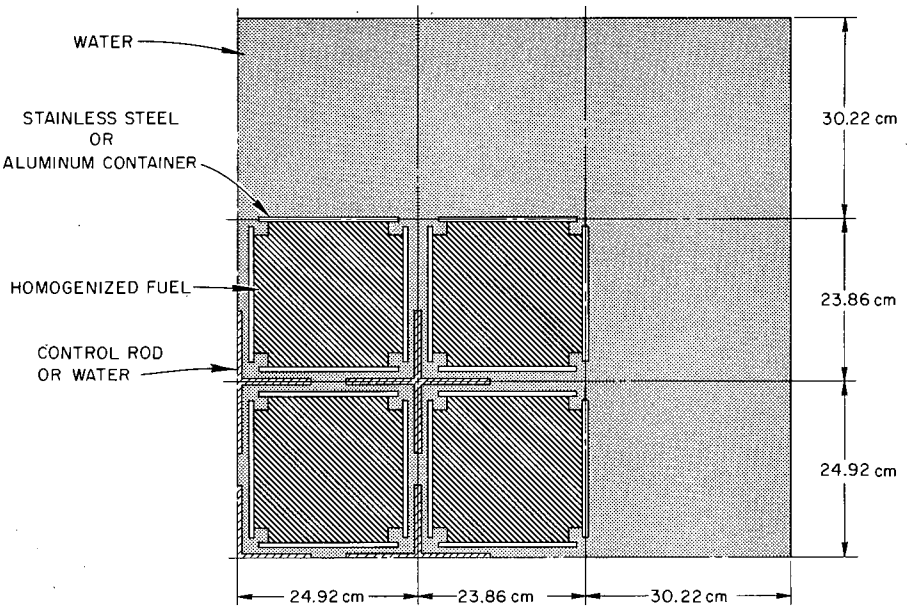

Fig. 16. Geometrical Model for One Quadrant of 16-Can Marty II or Marty III Cores.

UNCLASSIFIED
ORNL-LR-DWG 52970R2

ROD PATTERN	MARTY II		MARTY III	
	k_d EXP	k_s CALC	k_d EXP	k_s CALC
	1.043 ± 0.001	1.055	1.16 ± 0.02	1.180
	1.024 ± 0.001	1.030	1.13 ± 0.02	1.148
	1.0011 ± 0.0001	1.000	1.09 ± 0.01	1.099
	1.013 ± 0.001	1.021	1.11 ± 0.01	1.126

Comparison of Calculated and Experimental Multiplication Factors in Marty II and Marty III Critical Experiment.

Fig. 17. Comparison of Calculated and Experimental Multiplication Factors in Marty II and Marty III Critical Experiment.

It is apparent from Fig. 17 that the calculated multiplication factors are about 0.01 Δk higher than the measured values. In addition, although the calculated change in the multiplication factor resulting from a change in egg-crate material is in agreement with the measured effects within experimental errors, the calculations are again consistently higher than the measurements.

It should be noted, however, that the calculated and experimentally determined multiplication factors are not on the same basis. Multiplication factors obtained from Eq. 14 using a constant value for β are analogous to "dynamic" multiplication factors.[27] On the other hand, the calculated multiplication factors are "static" multiplication factors, k_s, obtained from the solution of Eqs. 1 or 3 for υ_c, where

$$k_s = \frac{\upsilon}{\upsilon_c} \quad . \tag{15}$$

For high-leakage, water-moderated cores, k_s and k_d values are expected to differ. To put the "experimental" k_d values on the same basis as the calculated k_s values would require the determination of so-called "effective betas" pertinent to each critical water height of the eight control-rod cases of Fig. 17. The tendency of the "effective betas" is to increase the value of the multiplication factors computed from Eq. 15 relative to multiplication factors based on the static value of the delayed neutron fraction.[27] This is in the direction of obtaining better agreement between theory and experiment.

5. RESULTS FOR CORE I FUEL ELEMENTS IN STAINLESS STEEL FUEL-ELEMENT CONTAINERS

Four-Group Cross Sections

Flux-averaged four-group cross sections for 4.2 wt % enriched UO_2, stainless steel, and water at room temperature are shown in Table 8. The stainless steel cross sections were based on the chemical analysis of fuel-tube steel. It should be pointed out that the normal tolerance on the

Table 8. Four-Group Macroscopic Cross Sections for Core I Pin-Cell Materials at 68°F

		Macroscopic Cross Section (cm^{-1})		
		4.2 wt %-Enriched UO_2	Stainless Steel	H_2O
Group 1	$\upsilon\Sigma_{f_1}$	0.01454	0	0
	Σ_{a1}	0.01034	0.00578	0.00028
	Σ_{tr1}	0.21774	0.25546	0.16196
	Σ_{12}	0.00144	0.00010	0.07550
	Σ_{13}	0	0	0.00012
	Σ_{14}	0	0	0
Group 2	$\upsilon\Sigma_{f2}$	0.04241	0	0
	Σ_{a2}	0.06243	0.01376	0
	Σ_{tr2}	0.37461	0.70838	0.56714
	Σ_{23}	0.00009	0	0.19268
	Σ_{24}	0	0	0.00196
Group 3	$\upsilon\Sigma_{f3}$	0.15422	0	0
	Σ_{a3}	0.11774	0.03010	0.00219
	Σ_{tr3}	0.36522	0.95875	0.59036
	Σ_{34}	0	0	0.28146
Group 4	$\upsilon\Sigma_{f4}$	1.09650	0	0
	Σ_{a4}	0.5787	0.21550	0.01810
	Σ_{tr4}	0.37580	0.83890	2.13820

manganese concentration in type 304 stainless steel can easily produce batches of steel that differ in thermal macroscopic absorption cross section by 5%. This variation in steel cross section in the N.S. SAVANNAH fuel tubing (9% of the core volume) could cause a variation of 0.01 Δk in the core multiplication factor.

Results for the stepwise homogenization of core I containing 4.2 wt % enriched UO_2 at 68°F using the cross sections of Table 8 are presented in the following sections. Results for other core variations (i.e., two-zone core, full-power core, and Zircaloy egg-crate core) are then presented only for the full-size core geometry.

Fuel-Pin-Cell Results

Flux distributions obtained from the solution to Eqs. 1 in the S-4 approximation[7] using the cross sections of Table 8 are shown in Fig. 18 for a fuel-pin cell. Because fission neutrons are born in group 1, this flux distribution is peaked in the UO_2 fuel. The flux distribution is reversed in the thermal group (group 4) because most of the slowing down occurs in the water and most of the thermal absorption occurs in the UO_2. It is evident from Fig. 18 that, on the small-scale level of a fuel-pin cell, the lethargy and space dependencies of the slowing-down flux are not separable. The deviations of group 2 and group 3 fluxes, which cover the energy region of the U^{238} resonances, from a "flat" distribution are not enough to invalidate our naive interpretation of the resonance-absorption integral of U^{238} in bulk UO_2.

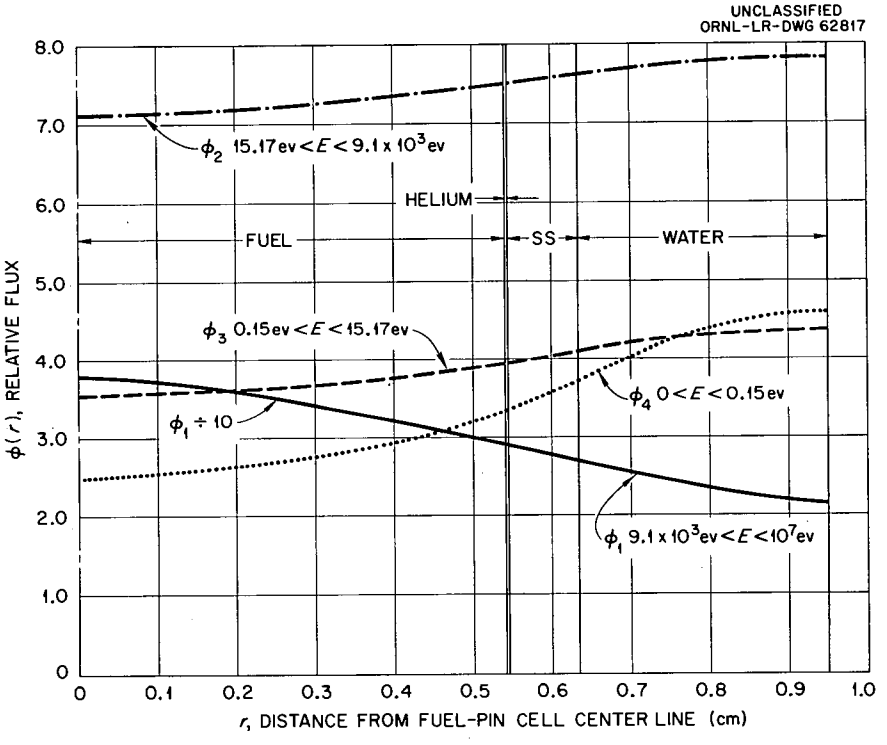

Fig. 18. S-4 Flux Distributions in N.S. SAVANNAH Core I Fuel-Pin Cell at 68°F.

The importance of nonthermal events in core I is revealed by the fuel-pin results of Fig. 18. Multiplication of the average fluxes in the UO_2 by the appropriate fission cross section in Table 8 gives the power distribution shown in Table 9. It should be noted that about 30% of the fissions occur at neutron energies in excess of 0.15 ev. Another interesting effect of nonthermal fissions concerns the spatial distribution of fissions throughout the UO_2 fuel pellets. Although Fig. 18 indicates that the maximum variation of the thermal flux across a UO_2 pellet is about 31%, the maximum variation of the power is only about 20%.

Table 9. Energy Distribution of Fission Events in a 4.2 wt % Core I Fuel-Pin Cell at 68°F

Group	Energy Interval (ev)	Fissions (%)
1	$9.1 \times 10^3 < E < 10^7$	10.5
2	$15.17 < E < 9.1 \times 10^3$	6.8
3	$0.15 < E < 15.17$	12.8
4	$0 < E < 0.15$	69.9

The four-group flux distributions shown in Fig. 18 permit the determination of flux and volume-averaged cross sections representing the entire fuel-pin cell. In a similar manner, appropriate homogenized four-group cross sections were obtained for that part of the fuel-bearing region containing stainless steel ferrules. The ferrule pin cell was approximated by the geometry of Fig. 7. The homogenized fuel-pin region with ferrules was then combined with the homogenized fuel-pin region without ferrules in the slab geometry of Fig. 8 to obtain homogenized four-group cross sections representing the entire fuel-pin region. In addition to reducing the complexity of the core geometry, this series of calculations revealed that elimination of the stainless steel ferrules (less than 0.3% of the core I volume) would increase core reactivity by $\Delta k = 0.01$. Another effect attributed to the ferrules is a periodic variation in power production along the axial direction of core I. On the average, the power

density produced by fuel in the ferrule-containing regions is about 8% lower than the power density produced by fuel in neighboring regions without ferrules.

Slab Fuel-Element Can-Cell Results

One-dimensional flux distributions within a fuel-element can cell containing control rods in the water channels between fuel cans are shown in Fig. 19. These results were obtained in the S-5 approximation using the water and steel cross sections shown in Table 8 and the homogenized fuel and 1.71 wt % boron-steel cross sections shown in Table 10. The boron in the boron-stainless steel rods is enriched to 92 wt % in B^{10}.

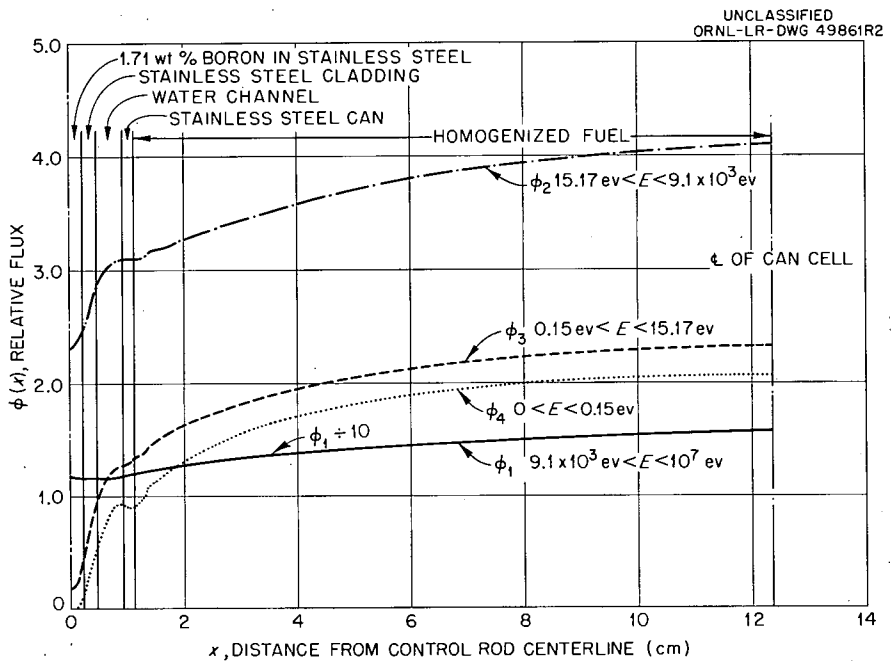

Fig. 19. S-5 Flux Distributions in N.S. SAVANNAH Core I Control-Rod Can Cell at 68°F.

The influence of the control rods on the nonthermal flux distributions is strikingly revealed in Fig. 19. It should be noted that the epithermal flux distribution $\phi_3(x)$, which provides the source for thermal

Table 10. Four-Group Macroscopic Cross Sections for Homogenized 4.2 wt %-Enriched Core I Fuel and 1.71 wt % Boron (92 wt % B^{10})-Stainless Steel at 68°F

		Macroscopic Cross Section (cm^{-1})	
		Homogenized Fuel	Boron Steel
Group 1	$\upsilon\Sigma_{f1}$	0.00569	0
	Σ_{a1}	0.00491	0.0187
	Σ_{tr1}	0.19726	0.2807
	Σ_{12}	0.03693	0.0001
	Σ_{13}	0.00006	0
	Σ_{14}	0	0
Group 2	$\upsilon\Sigma_{f2}$	0.13200	0
	Σ_{a2}	0.02111	0.3726
	Σ_{tr2}	0.52149	0.7248
	Σ_{23}	0.10884	0
	Σ_{24}	0.00110	0
Group 3	$\upsilon\Sigma_{f3}$	0.04625	0
	Σ_{a3}	0.04024	4.3723
	Σ_{tr3}	0.76487	0.9702
	Σ_{34}	0.16082	0
Group 4	$\upsilon\Sigma_{f4}$	0.27390	0
	Σ_{a4}	0.18115	24.9806
	Σ_{tr4}	1.53410	0.9006

neutrons, is very far from being a "flat" distribution. Also the perturbing influence of the water channel on the four-group fluxes and the thermal flux, in particular, may be seen.

The strong nonthermal absorption properties of the N.S. SAVANNAH control rods may also be illustrated by the energy distribution of neutron absorptions in the control rod as shown in Table 11. According to these results, only about one-fourth of the neutrons absorbed by the N.S. SAVANNAH control rods are "thermal" neutrons. The strong nonthermal absorption properties of boron are also exhibited by Fig. 20, which shows the relative control-rod worth as a function of enriched boron concentration. The results of Fig. 20 were obtained by repeating the fuel-element cancell S-5 calculations for various amounts of boron in the control rod.

Table 11. Energy Distribution of Control-Rod Absorptions

Group	Energy Interval (ev)	Control Rod Absorptions (%)
1	$9.1 \times 10^3 < E < 10^7$	8
2	$15.17 < E < 9.1 \times 10^3$	29
3	$0.15 < E < 15.17$	37
4	$0 < E < 0.15$	26

Although the control rod is "thermally black" for enriched boron concentrations of about 0.1 wt %, there is considerable rod-worth increase for higher boron concentrations. Figure 20 also suggests that further rod-worth increases are possible for boron concentrations in excess of the 1.71 wt % boron content of the rods as fabricated.

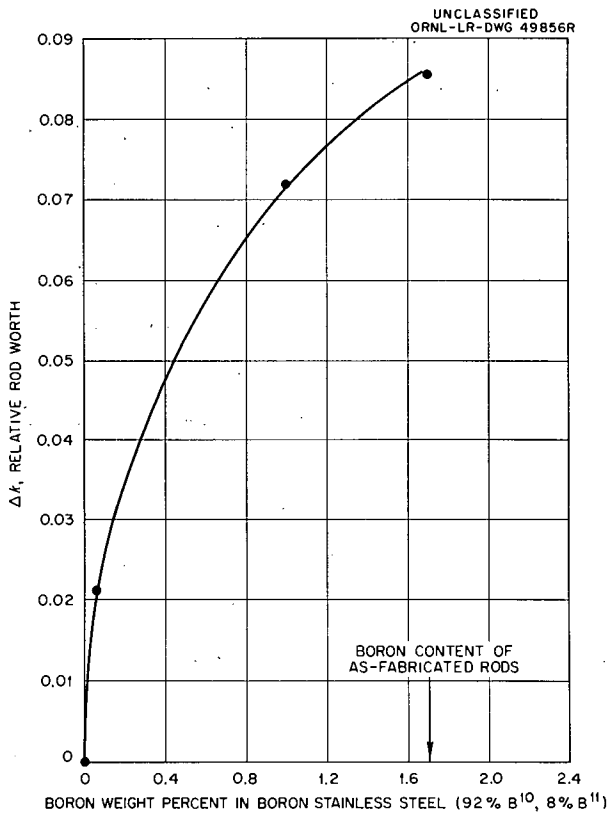

Fig. 20. Relative N.S. SAVANNAH Core I Rod Worth vs Rod Boron Content at 68°F, S-5 Results.

The main purpose of the slab geometry control-rod calculation is to generate transport theory values for the current per unit flux (Eq. 12) at the control-rod surface. Values obtained from Fig. 19 are shown in Table 12. Also shown in Table 12 are the customary "black body" boundary condition values for the current per unit flux according to diffusion and transport theories. The transport theory value results from the solution to the Milne problem

Table 12. Current per Unit Flux Values at a Control-Rod Surface According to Fig. 19 Compared with "Black Body" Values

Group	Energy Interval (ev)	J/ϕ at Rod Surface
1	$9.1 \times 10^3 < E < 10^7$	−0.0058
2	$15.17 < E < 9.1 \times 10^3$	−0.077
3	$0.15 < E < 15.17$	−0.309
4	$0 < E < 0.15$	−0.389
	"Black-body" diffusion theory	−0.50
	"Black-body" transport theory	−0.47

which, as was shown in Section 3, is quite adequately treated by the S-5 approximation used here.

Applying the transport-theory boundary conditions of Table 12 at the surface of the control rod and repeating the calculation of four-group fluxes in the geometry of Fig. 19 with diffusion theory (Eqs. 3) yielded a multiplication factor some 0.01 Δk less than the S-5 result. This shows that a simple current per unit flux boundary condition cannot always rectify diffusion theory, since much more information is contained in transport theory than can be expressed in such a boundary condition. Rather than adjust the control-rod boundary conditions until diffusion theory gives the same multiplication factor as S_n transport theory, we have retained the above-described unambiguous method for determining the boundary conditions and have adjusted diffusion-theory multiplication factor values by the results of a one-dimensional fuel-element can-cell comparison of diffusion theory and S_n transport theory. Thus, we have assumed that the ratio between diffusion-theory and transport-theory multiplication factors found for one-dimensional calculations will retain the same value in two dimensions.

Although the diffusion-theory calculations of control-rod multiplication factors need to be corrected by about $\Delta k = 0.01$, little or no adjustment needed to be made to the diffusion-theory power distribution. Figure 21 shows a comparison of the calculated power distributions according to S-5 and diffusion theories for a one-dimensional fuel-element can cell.

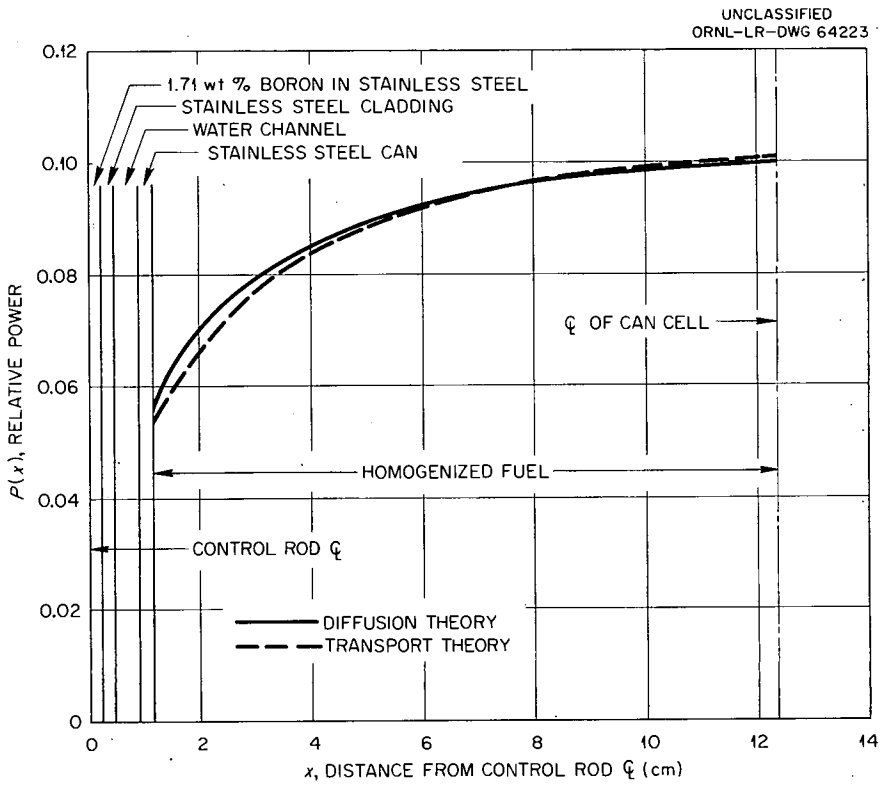

Fig. 21. Comparison of Diffusion-Theory and Transport-Theory Power Distributions for Core I Control-Rod Can Cell at 68°F.

Similar slab-geometry data for the case when Zircaloy followers are present in the channels between cans are shown in Fig. 22. These results illustrate the severe thermal-flux peaking caused by water channels; the importance of this peaking on the flux level in the egg-crate material is evident. In all calculations involving Zircaloy followers, the water channels have been characterized by well-moderated cross sections. Although this treatment may not give the best results for the thermal-flux distribution in the channel region,[28,29] the method was consistently applied. The effect on core reactivity of a Zircaloy egg crate relative to a stainless steel egg crate should thus be fairly represented.

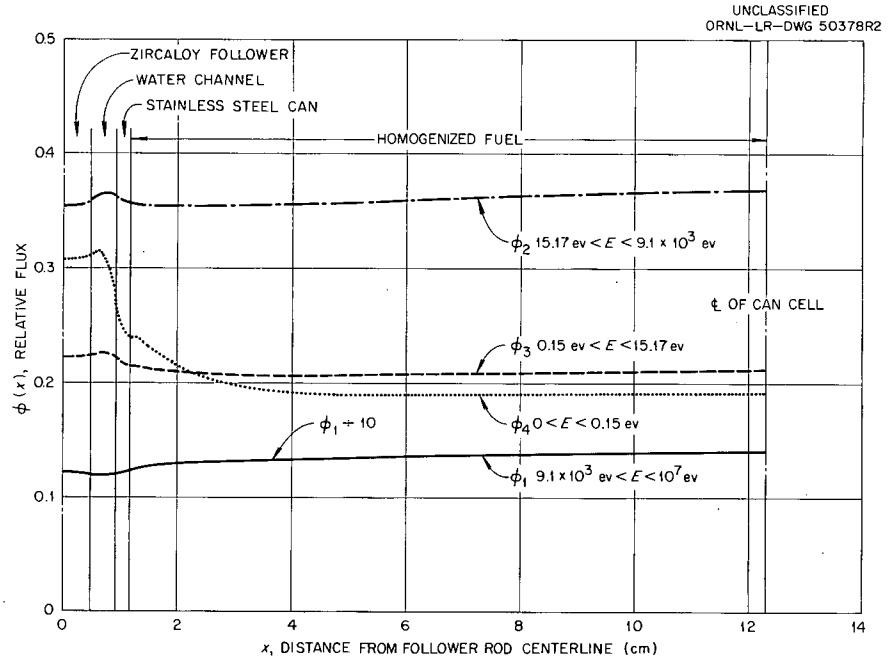

Fig. 22. S-5 Flux Distributions in N.S. SAVANNAH Core I Follower Can Cell at 68°F.

Two-Dimensional Fuel-Element Can-Cell Results

The main purpose of a two-dimensional fuel-element can-cell calculation was to further reduce the complexity of the core so that the full-sized core (32 fuel elements and 21 control rods or followers or both) could be handled within the space-point limitations of the PDQ code.[6] It will be remembered that, to simplify the core geometry, it was found expedient to combine the water channel and egg-crate material into a single homogeneous medium (Region 3 in Fig. 14) on the basis of flux distributions computed in the geometry of Figs. 12 and 13.

It is clear from the one-dimensional results that the flux distribution in the channel region depends acutely on whether a control rod (Fig. 19) or a follower (Fig. 22) is in the channel between fuel-element containers. The dependence of the homogenized channel properties on these flux conditions is displayed by the cross sections of Table 13. In particular, the thermal absorption cross sections, Σ_{a4}, shown in Table 13 reflect the fact that, when the rods are present, the average thermal flux

Table 13. Homogenized Four-Group Channel Constants for Stainless Steel Egg-Crate Core at 68°F

		Macroscopic Cross Section (cm^{-1})		Diffusion Coefficient (cm)	
		Channel Near Control Rods	Channel Near Followers	Channel Near Control Rods	Channel Near Followers
Group 1	Σ_{a1}	0.00219	0.00242	1.74786	1.71893
	Σ_{12}	0.04999	0.04678		
Group 2	Σ_{a2}	0.00485	0.00532	0.54563	0.54156
	Σ_{23}	0.12757	0.12081		
Group 3	Σ_{a3}	0.01282	0.01288	0.48163	0.48117
	Σ_{34}	0.17422	0.17363		
Group 4	Σ_{a4}	0.09099	0.08626	0.24019	0.22569

in the egg crate is higher than the average thermal flux in the water channel and vice versa for the case when followers are present between fuel containers.

The power generated at the center of each fuel-pin location relative to the average power is shown in Fig. 23 for followers in the core and in Fig. 24 for control rods in the core. These figures serve to indicate how the power distribution varies with conditions in the channel around a fuel element.

Two-Dimensional Full-Core Results

One way of illustrating the detail contained in the analysis used here is shown in Fig. 25, which presents the average four-group fluxes in each of the regions of core I (4.2 wt % U^{235}, single fuel zone) at the operating temperature of 508°F. All fluxes in Fig. 25 have been normalized to unity in the UO_2 region. The heterogeneous nature of the N.S. SAVANNAH core I design with respect to both fast- and thermal-neutron fluxes is quite evident from Fig. 25 and justifies a detailed geometrical model.

The main influence of moderator temperature is on the thermal-flux distr bution, as shown in Fig. 26, which compares the thermal-flux

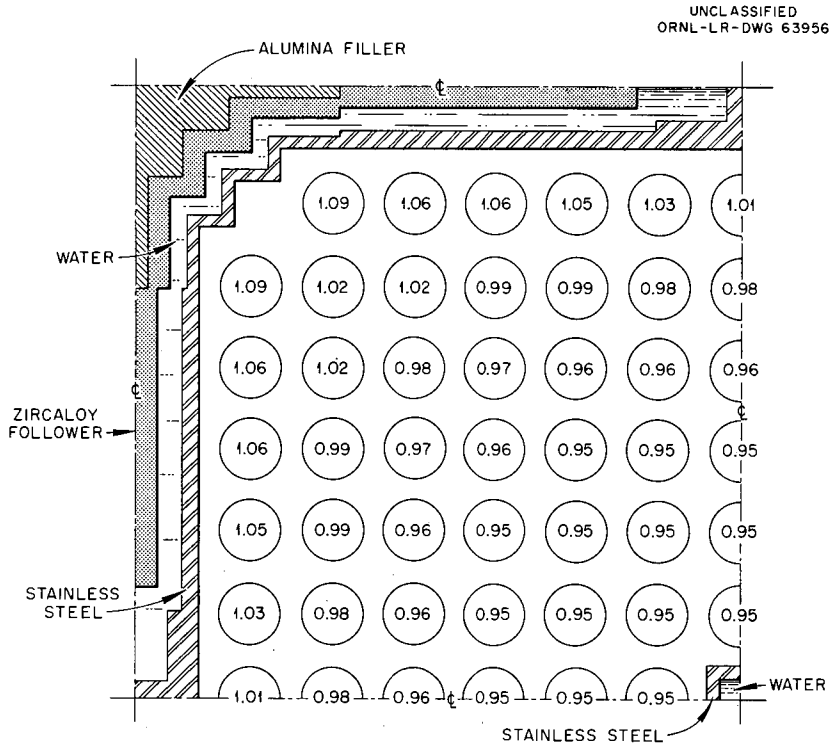

Fig. 23. Power at the Center of Each Fuel Pin Relative to Average Power in a Quadrant of a Follower Can Cell at 68°F. The average power is normalized to unity.

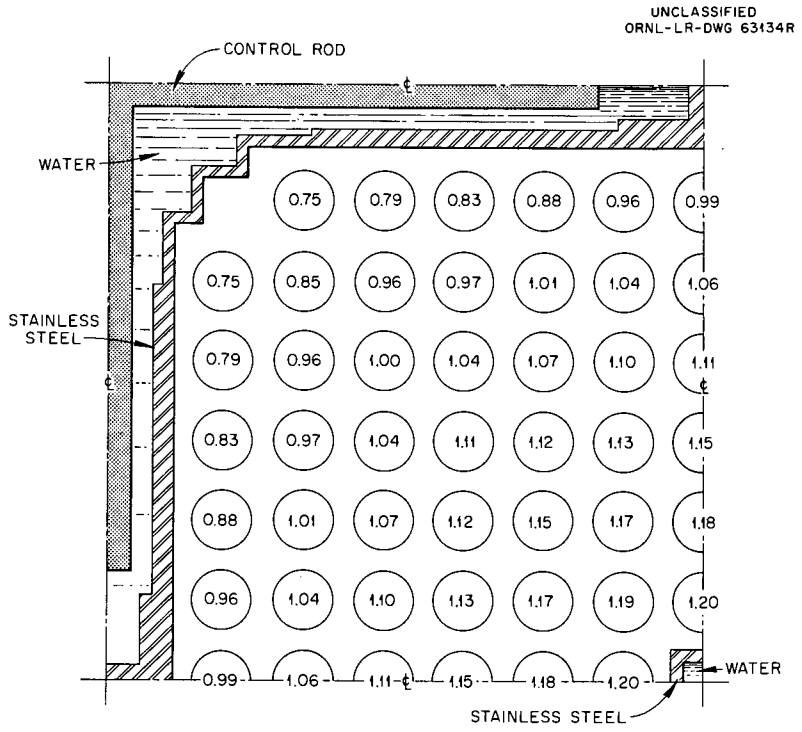

Fig. 24. Power at the Center of Each Fuel Pin Relative to Average Power in a Quadrant of a Control-Rod Can Cell at 68°F. The average power is normalized to unity.

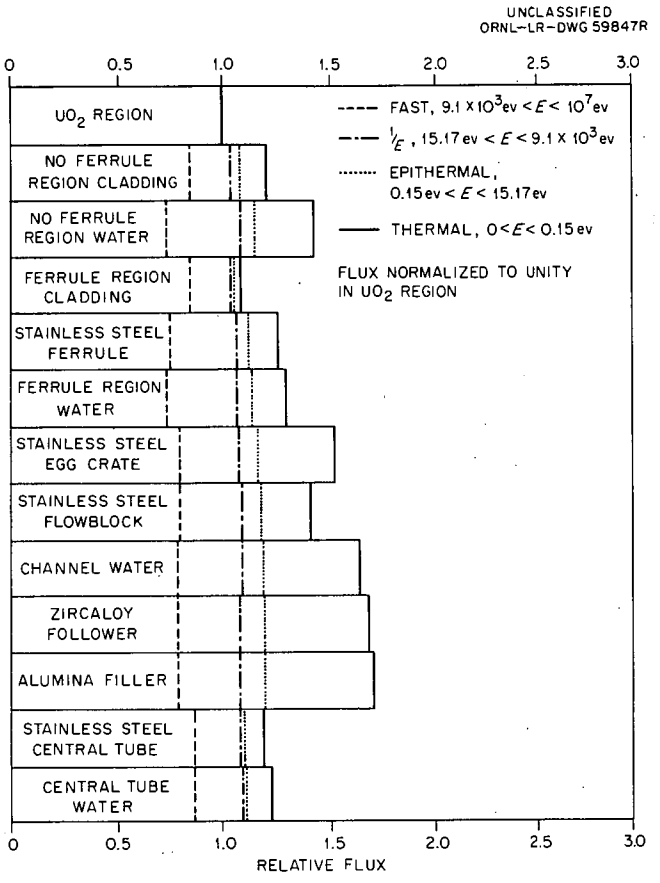

Fig. 25. Relative Four-Group Fluxes in N.S. SAVANNAH Core I Components at 508°F.

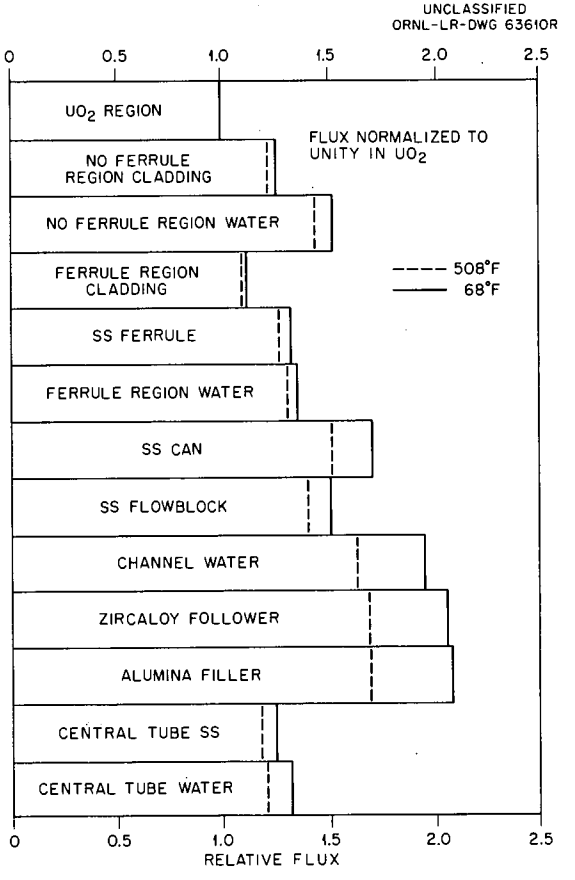

Fig. 26. Relative Thermal Fluxes in N.S. SAVANNAH Core I Components at 68°F and 508°F.

distribution at room temperature (68°F) with that at operating temperature (508°F). The effect of increasing the moderator temperature is to cause a general flattening of the thermal-flux distribution.

Calculated static multiplication factors for N.S. SAVANNAH core I (with either all followers or all control rods in the core) are shown in Table 14. Also included in Table 14 are static multiplication factors at 68°F inferred from the zero-power experiment.[5] The measured static multiplication factors should have an experimental uncertainty of about $\Delta k = 0.01$ associated with them.[30] Interpretation of the critical water-height data to obtain the static multiplication factor of the fully reflected core containing followers is perhaps uncertain by an additional 1% Δk. Thus agreement of the calculation with the zero-power experiment is quite satisfactory.

Table 14. Calculated and Measured Static Multiplication Factors for Core I

	Static Multiplication Factors		
	Calculated		Measured, Two Zone
	One Zone	Two Zone	
Followers at 68°F	1.132	1.135	1.123[a]
Rods at 68°F	0.972	0.978	0.980[b]
Followers at 508°F, zero-power operation	1.087	1.090	
Rods at 508°F, zero-power operation	0.889	0.895	
Followers at 508°F, full-power operation	1.079	1.082	
Rods at 508°F, full-power operation	0.881	0.887	

[a]This value represents the latest interpretation of the water-height data; R. Webb, Babcock & Wilcox Company, personal communication.

[b]See ref. 5.

The calculated multiplication factors given in Table 14 resulted from two-dimensional r-z geometry calculations. In these r-z calculations, the core was treated as a single homogeneous medium that was homogenized on the basis of a two-dimensional x-y geometry calculation using the geometry shown in Fig. 14. The radius of the cylindrical core (78.44 cm) was chosen to give the same area as contained in the four core regions of Fig. 14. The top and bottom end reflectors consisted of a 2-in. region containing 50% H_2O and 50% steel, simulating the top and bottom grid plates, followed by an essentially infinite water region. The main effect of adding these end reflectors is the removal of the power peaking that would occur near a pure-water reflector, as is illustrated in Fig. 27. Unfortunately, flux measurements[5] were not made sufficiently close to the axial reflector region to check the influence of the grid plate on the thermal-flux distribution.

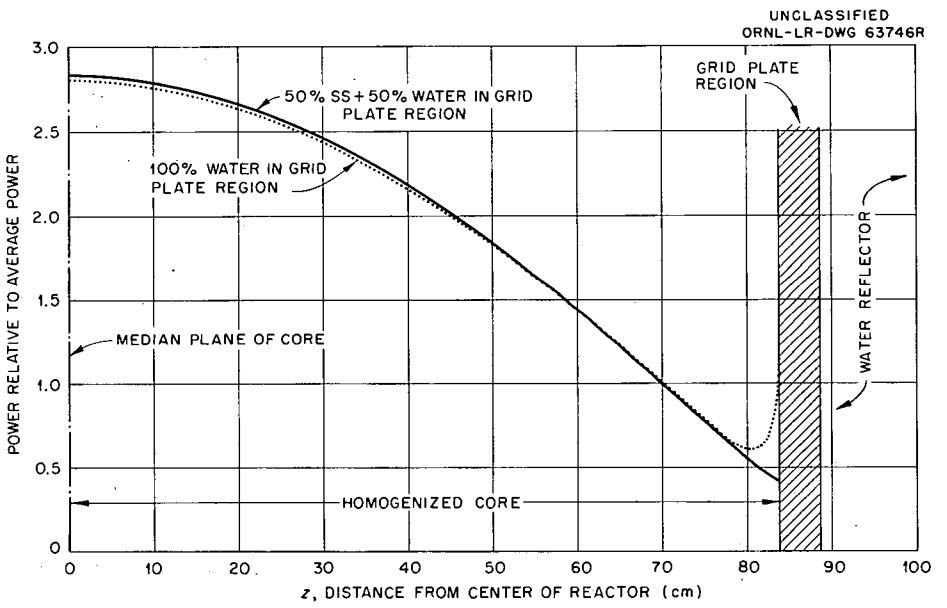

Fig. 27. Power Along Axis of N.S. SAVANNAH Core I at 68°F Relative to Average Power.

6. COMPARISON OF ZIRCALOY AND STAINLESS STEEL AS FUEL-CONTAINER MATERIALS FOR CORE I FUEL ELEMENTS

Comparison of Static Multiplication Factors at 68°F

Calculations for a Zircaloy egg-crate core were identical to those for a stainless steel egg-crate core except that the egg crate was characterized by Zircaloy cross sections rather than by stainless steel cross sections. Zircaloy and stainless steel egg-crate cross sections at 68°F are compared in Table 15.

Table 15. Four-Group Macroscopic Fuel-Container Cross Sections at 68°F

		Macroscopic Cross Section (cm^{-1})	
		Stainless Steel	Zircaloy
Group 1	Σ_{a1}	0.00578	0.00135
	Σ_{tr1}	0.25546	0.26345
	Σ_{12}	0.00010	0.00009
Group 2	Σ_{a2}	0.01376	0.01826
	Σ_{tr2}	0.70838	0.26345
	Σ_{23}	0	0
Group 3	Σ_{a3}	0.03010	0.00127
	Σ_{tr3}	0.95875	0.26345
	Σ_{34}	0	0
Group 4	Σ_{a4}	0.21050	0.00708
	Σ_{tr4}	0.83890	0.26860

To maintain equal strength with respect to egg-crate deflection, it was initially estimated that a 0.122-in. Zircaloy egg-crate thickness was required. Subsequent stress calculations[31] have indicated that a Zircaloy egg-crate thickness of 0.140 in. is required to give the same strength as is inherent in 0.94-in.-thick stainless steel egg crates. However, calculations with the two-dimensional geometry of Figs. 12 and 13 reveal

essentially no dependence of the multiplication factor on egg-crate thickness for Zircaloy egg crates in the thickness range 0.122 to 0.140 in.

Zircaloy egg-crate core calculations were performed for two fuel enrichments, 3.0 and 4.2 wt % U^{235}. Results for cores containing either all followers or all control rods are presented in Fig. 28, along with the stainless steel egg-crate results at a fuel enrichment of 4.2 wt % U^{235}. The shape of the curve between fuel enrichments of 3.0 and 4.2 wt % U^{235} was taken from the results of a previous survey[32] using a somewhat simpler analytical method. It is apparent from Fig. 28 that substitution of a Zircaloy egg crate for the present stainless steel egg crate would increase the reactivity of 4.2 wt % U^{235} core I fuel elements by about 6% Δk.

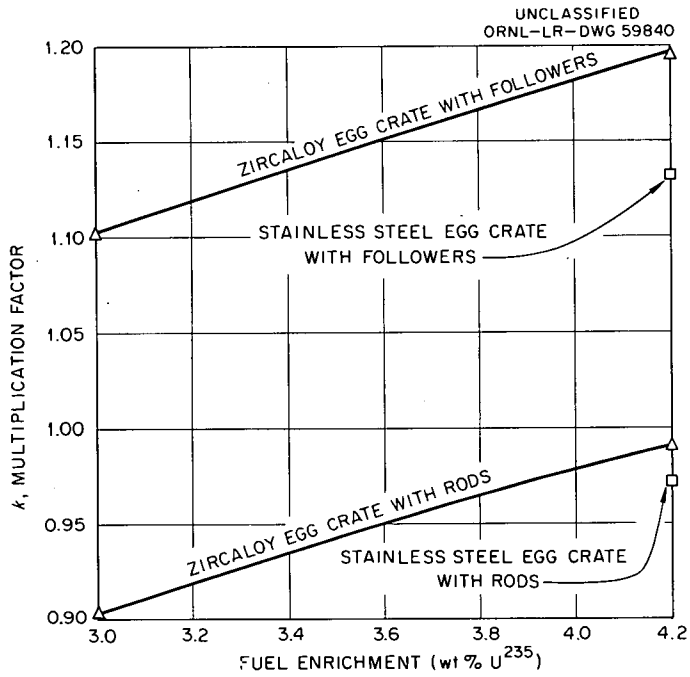

Fig. 28. Calculated Multiplication Factors for Core I Type Fuel Elements in Zircaloy and in Type 304 Stainless Steel Egg Crates at Beginning of Life, 68°F.

The worth of the 21 control rods may be obtained from Fig. 28 by subtracting the multiplication factor of the core with rods from the multiplication factor of the core with followers. The rod worth defined in this

fashion is remarkably independent of enrichment in the Zircaloy egg-crate core, at least in the enrichment range 3.0 to 4.2 wt % U^{235}. As presaged by calculations on the Marty II and Marty III critical experiments comparing aluminum and stainless steel egg crates (Section 4), the rod worth in the Zircaloy egg-crate core is seen to be some 4% Δk greater than the rod worth in the stainless steel egg-crate core; however, this rod worth is barely enough to hold down 4.2 wt %-enriched core I fuel elements. To obtain the same shutdown margin as is present in the stainless steel egg-crate core, the Zircaloy egg-crate core would require a 3.9 wt % U^{235} fuel enrichment. Since control rods are worth more in a Zircaloy egg crate, a safer shutdown criterion would prescribe the same shutdown margin with the central control rod stuck out of the core as is present in the stainless steel egg-crate core. This one-stuck-rod criterion for the shutdown margin requirement would be satisfied by an enrichment of about 3.86 wt % U^{235} in the Zircaloy egg-crate core.

Comparison of Static Multiplication Factors at Full Power

Calculated multiplication factors for full-power conditions at the beginning of core life are shown in Fig. 29. Comparison of Figs. 28 and 29 reveals an over-all temperature deficit (reactivity difference between the room temperature core and the full-power core) of 5.3% Δk for the stainless steel egg-crate core and 5.4% Δk for the Zircaloy egg-crate core. Also from Fig. 29 it is apparent that a fuel enrichment of 3.38 wt % U^{235} in Zircaloy egg crates would have the same initial hot reactivity (and, therefore, about the same reactivity lifetime) as 4.2 wt % U^{235} fuel in stainless steel egg crates. A fuel enrichment to 3.86 wt % U^{235} in Zircaloy egg crates (this enrichment satisfies the one-stuck-rod shutdown criterion) would have 4% Δk more hot reactivity available for burnup than is available in a stainless steel egg-crate core containing 4.2 wt % U^{235} fuel.

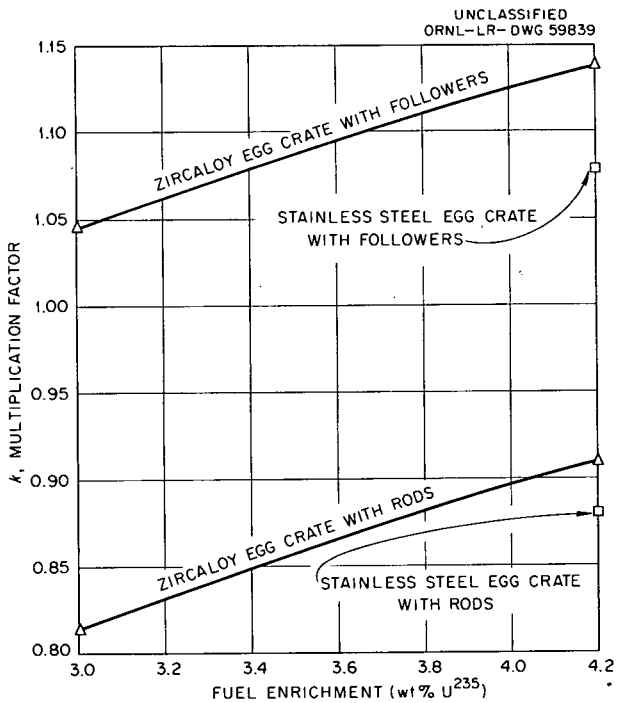

Fig. 29. Calculated Multiplication Factors for Core I Type Fuel Elements in Zircaloy and Type 304 Stainless Steel Egg Crates at Beginning of Life for Full-Power at 508°F and No Xenon.

Comparison of Power Distributions

In addition to core reactivity and control-rod worth, the egg-crate material affects the power distribution. The general features of the influence of egg-crate material on core power distributions is revealed by Fig. 30. The horizontal power distributions shown in Fig. 30 represent the power-to-average power ratio along the centerline of the row of fuel pins nearest the egg crate along the profile shown in the upper righthand corner. It may be seen that, although the Zircaloy structure produces greater power peaking near the water channels, the net peak-to-average ratio for the entire core is essentially the same for both Zircaloy and stainless steel egg-crate cores.

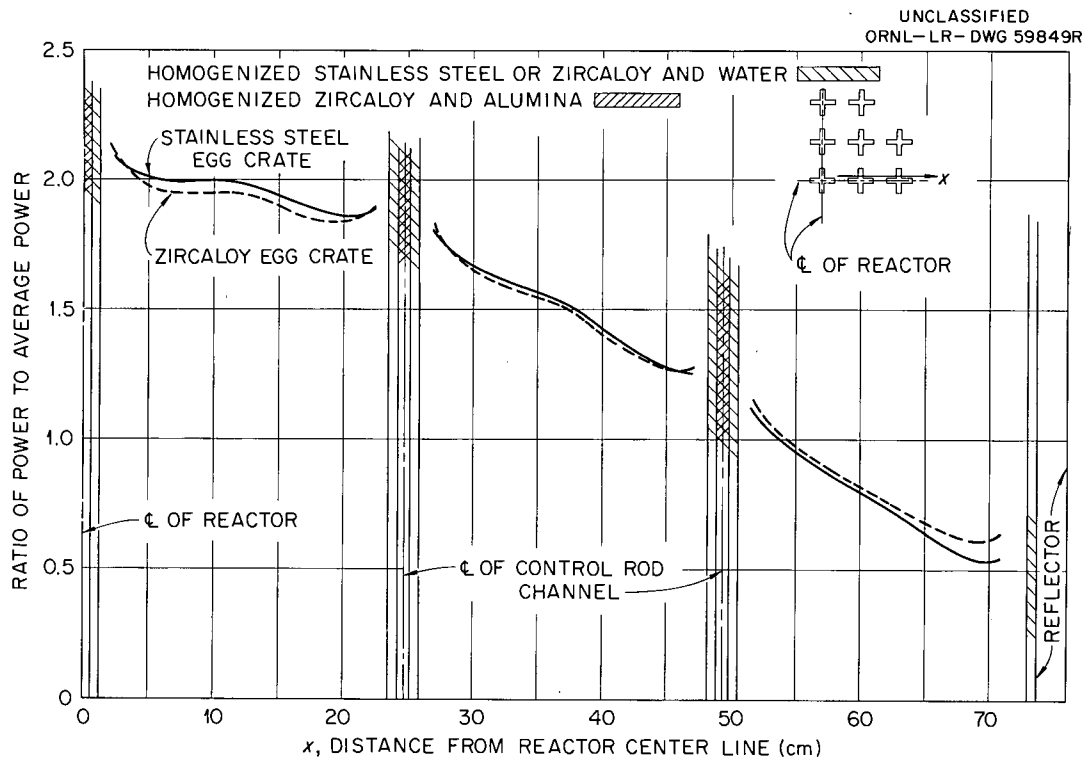

Fig. 30. Comparison of Power Distributions for 4.2 wt % U^{235} Core I Fuel Elements in Zircaloy and in Type 304 Stainless Steel Egg Crates at 508°F.

7. REACTIVITY LIFETIME COMPARISON OF CORES WITH ZIRCALOY OR STAINLESS STEEL FUEL CONTAINERS

To complete the comparison of Zircaloy and stainless steel as fuel-container materials in N.S. SAVANNAH core I, simple one-dimensional radial burnup calculations were performed by use of the CANDLE code.[33] Homogenized four-group cross sections representing the core region at the beginning of life were obtained from the full-core, two-dimensional calculations (geometry of Fig. 14 with followers present). Plutonium isotopes and fission products were assumed to be exposed to the same flux levels as seen by the UO_2.

With the exception of xenon and samarium, fission products were treated as a single isotope ("fissium") having a resonance absorption integral of 214 barns and a thermal absorption cross section of 43 barns at 2200 m/sec. These values are based on a study by Nephew.[34]

Dilute resonance integrals for plutonium isotopes were used throughout the lifetime calculation. Resonance integrals and 2200 m/sec cross sections used for plutonium isotopes, xenon, samarium, and "fissium" are listed in Table 16. Multigroup cross sections generated from the resonance integrals are included in Appendix 2.

Table 16. Cross-Section Data Used in N.S. SAVANNAH Lifetime Studies

	2200 m/sec Cross Sections (barns)		Resonance Integrals (barns)	
	Absorption	Fission	Absorption	Fission
Pu^{239}	1026	742	789	510
Pu^{240}	285	0	8700	0
Pu^{241}	1400	1025	1228	923
Xe	2.7×10^6	0	0	0
Sm	4.08×10^4	0	0	0
Fissium	43	0	214	0

The full-power (63-Mw) multiplication factor as a function of time calculated with CANDLE for an initial loading of 4.2 wt % U^{235} fuel is shown in Fig. 31 for both stainless steel and Zircaloy egg-crate cores. Note that initial one-dimensional multiplication factors using CANDLE are in excellent agreement with the heterogeneous, two-dimensional values from PDQ (Fig. 29). The initial drop in reactivity is due to the buildup of equilibrium xenon (1.2% Δk). Following the buildup of equilibrium samarium (~0.3 years), the multiplication factor as a function of time appears to be quite linear with essentially the same slope for both cores.

A xenon override option in CANDLE (as well as a hand calculation estimate) reveals a maximum xenon override of about 0.08% Δk over and above the reactivity tied up in equilibrium xenon. Assuming that the end of core life occurs when maximum xenon cannot be overridden, the stainless steel egg-crate core would last 1.6 full-power years, while the Zircaloy egg-crate core would last 3.2 full-power years, or twice as long as the stainless steel egg-crate core.

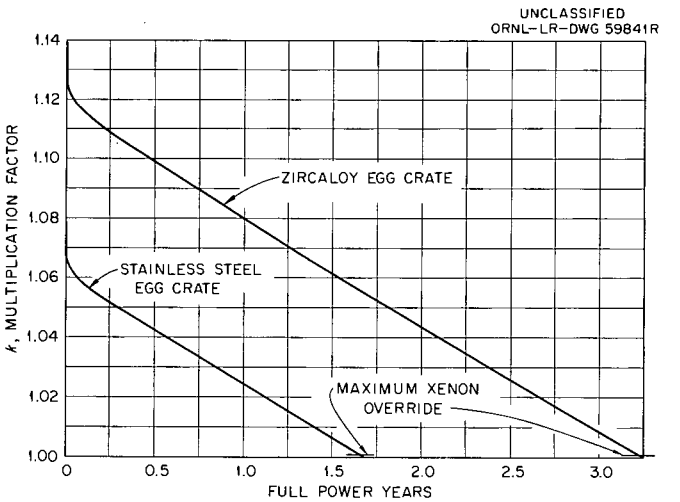

Fig. 31. Calculated Reactivity Lifetime of 4.2 wt % U^{235} Core I Fuel in Zircaloy and in Type 304 Stainless Steel Egg Crates at a Power Level of 63 Mw.

As pointed out previously, for the same fuel enrichment, a Zircaloy egg-crate core would not have as large a control-rod shutdown margin as a stainless steel egg-crate core. To obtain the same shutdown margin with the central control rod stuck out of the core as is available in a 4.2 wt % U^{235} stainless steel egg-crate core, a Zircaloy egg-crate core would require about 3.86 wt % U^{235} fuel. Using the results of Fig. 29 to estimate the initial hot reactivity for this enrichment, and the slope of the burnup curve from Fig. 31, such a core (3.86 wt % U^{235} in Zircaloy egg crates) is estimated to have a reactivity lifetime about 0.9 full-power years greater than a stainless steel egg-crate core containing 4.2 wt % U^{235} fuel. This additional core life represents an estimated 30% reduction of fuel-cycle costs.[35]

Core inventories of U^{235}, Pu^{239}, and Pu^{241} (which are important in fuel-cycle economics) are shown in Figs. 32, 33, and 34, respectively. These results apply to an initial one-zone loading of 4.2 wt % U^{235} fuel in either stainless steel of Zircaloy egg crates. The burnup of U^{235} (Fig. 32) is fairly linear, with a slope of about 25 kg per full-power year. The buildup of Pu^{239} (Fig. 33) occurs at a rate of about 8 kg per full-power year during the first full-power year and at the rate of about

6 kg per full-power year during the second year of full-power operation. The buildup of Pu^{241} (Fig. 34) is quadratic in nature, depending as it does on the buildup of intermediate isotopes of plutonium.

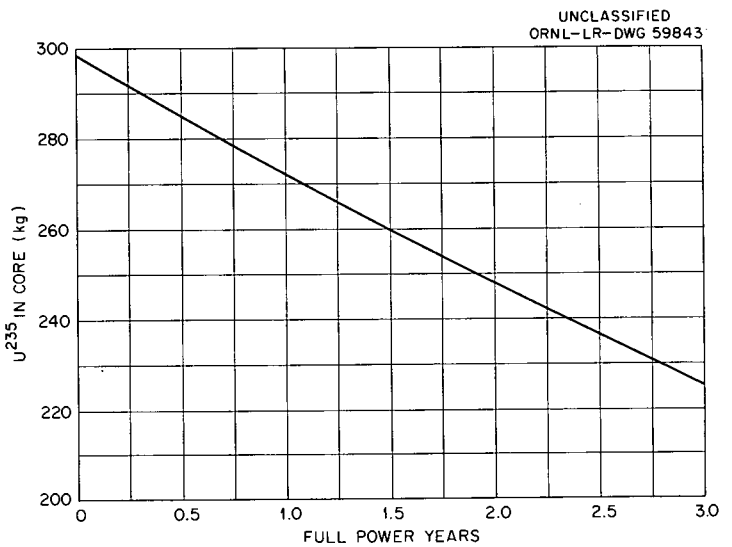

Fig. 32. Burnup of U^{235} in 4.2 wt % U^{235} Core I Fuel Elements at a Power Level of 63 Mw.

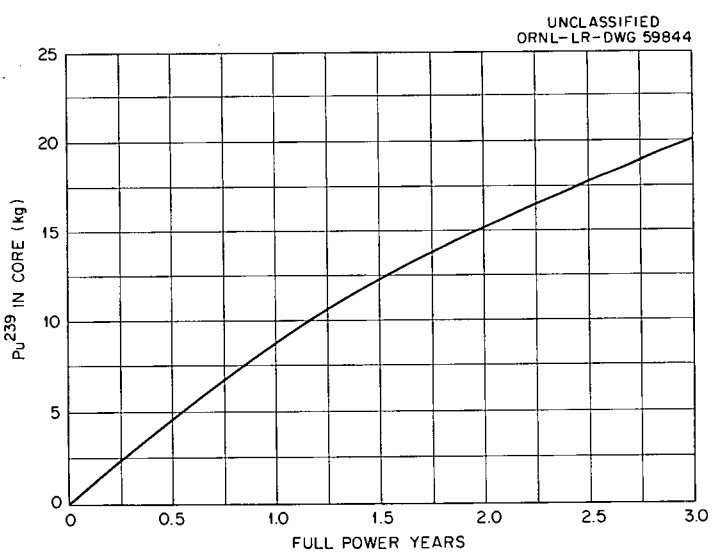

Fig. 33. Buildup of Pu^{239} in 4.2 wt % U^{235} Core I Fuel Elements at a Power Level of 63 Mw.

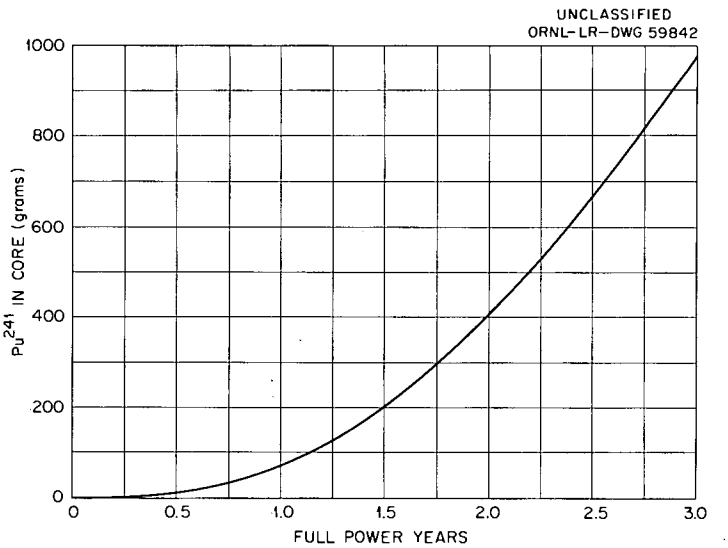

Fig. 34. Buildup of Pu^{241} in 4.2 wt % U^{235} Core I Fuel Elements at a Power Level of 63 Mw.

ACKNOWLEDGMENTS

The early stages of this study were aided by many tedious hand calculations perfomed by Russ Aven and Martha Beatty. We are indebted to Verner Anderson, who wrote subsidiary codes that were helpful in this study, especially the S-5 version of the SNG code. Betty Maskewitz was most helpful in adjusting the CANDLE code to meet our needs. Finally, we are thankful to Russel Ball for his cooperation in furnishing and discussing experimental data on the NMSR critical experiments.

REFERENCES

1. R. M. Ball, A. L. MacKinney, and J. H. Mortenson, "Marty Critical Experiments Summary of 4% Enriched UO_2 Cores for NMSR," BAW-1216 (May 1961).

2. "Transcripts of Symposia on Economic Comparison of Zirconium and Stainless Steel in Nuclear Power Reactors; New York, February 13, 1958, and Pittsburgh, March 11, 1958," NP-7261.

3. N. Beecher and M. Benedict, "Which for Minimum Fuel Cost – Zircaloy or Stainless Clad?" Nucleonics 17 (7), 64 (1959).

4. G. E. Kulynych, "Nuclear Merchant Ship Reactor Final Safeguards Report, Description of the N.S. SAVANNAH," BAW-1164, Vol. I (June 1960).

5. R. M. Ball and A. L. MacKinney, "Nuclear Merchant Ship Reactor Zero Power Test, Core I," BAW-1202 (July 1960).

6. G. G. Bilodeau et al., "PDQ, An IBM-704 Code to Solve the Two-Dimensional Few-Group Neutron-Diffusion Equations," WAPD-TM-70 (1957).

7. B. G. Carlson and G. I. Bell, "Solution of the Transport Equation by the S_n Method," Proceedings Second International Conference on Peaceful Uses of Atomic Energy, Geneva, Vol. 16, 535 (1958).

8. B. G. Calson, "The S_n Method and the SNG and SNK Codes," LASL T-1-159 (January 26, 1958).

9. A. M. Weinberg and E. P. Wigner, The Physical Theory of Neutron Chain Reactions, pp. 332 ff, The University of Chicago Press, Chicago, 1958.

10. H. D. Brown, "Neutron Energy Spectra in Water," DP-64 (February 1956).

11. D. J. Hughes and R. B. Schwartz, "Neutron Cross Sections," BNL-325 (July 1, 1958).

12. R. W. Deutsch, "Temperature Dependence of the Thermal Diffusion Length in Water," Nuclear Sci. & Eng. 1, 252 (1956).

13. C. D. Petrie, M. L. Storm, and P. F. Zweifel, "Calculation of Thermal Group Constants for Mixtures Containing Hydrogen," Nuclear Sci. & Eng. 2, 728 (1957).

14. C. L. Davis, J. M. Bookston, and B. E. Smith, "GNU, A Multigroup One-Dimensional Diffusion Program for the IBM-704," GMR-101 (November 12, 1957).

15. A. L. Boch et al., "A Conceptual Design of a Pressurized-Water Reactor," ORNL-1613 (November 2, 1955), p. 125.

16. L. Cranberg and J. S. Levin, "Inelastic Neutron Scattering by U^{238}," Phys. Rev. 109, 2063 (1958).

17. R. B. Day, "Gamma Rays from Neutron Inelastic Scattering," Phys. Rev. 102, 767 (1956).

18. V. E. Scherrer, B. A. Allison, and W. R. Faust, "Gamma Radiation from Interaction of 3.2-Mev Neutrons with Various Materials," Phys. Rev. 96, 386 (1954).

19. B. Jennings, J. B. Weddell, and R. L. Hellens, "Inelastic Scattering of 4.3-Mev Neutrons by Fe^{56}," Phys. Rev. 95, 636 (1954).

20. J. R. Beyster, M. Walt, and E. W. Salmi, "Interaction of 1.0-, 1.77-, 2.5-, 3.25-, and 7.0-Mev Neutrons with Nuclei," Phys. Rev. 104, 1319 (1956).

21. R. L. Macklin and H. S. Pomerance, "Resonance Capture Integrals," Progress in Nuclear Energy, Series I, Physics and Mathematics, p. 179, McGraw-Hill, New York, 1956.

22. E. Hellstrand, "Measurements of the Effective Resonance Integral in Uranium Metal and Oxide in Different Geometries," J. Appl. Phys. 28, 1493 (1957).

23. J. A. Thie, "A Simple Analytical Formulation of the Dancoff Correction," Nuclear Sci. & Eng. 5, 75 (1959).

24. E. Hellstrand, P. Blomberg, and S. Horner, "The Temperature Coefficient of the Resonance Integral for Uranium Metal and Oxide," Nuclear Sci. & Eng. 8, 497 (1960).

25. A. M. Weinberg and E. P. Wigner, op. cit., pp. 253–66.

26. Ibid., p. 262.

27. E. E. Gross and J. H. Marable, "Static and Dynamic Multiplication Factors and their Relation to the Inhour Equation," Nuclear Sci & Eng. 7, 281 (1960).

28. W. B. Wright and F. Feiner, "Note on Position Dependent Spectra," Nuclear Sci. & Eng. 6, 81 (1959).

29. G. P. Calame, "A Few-Group Theory of Water Gap Peaking," Nuclear Sci. & Eng. 8, 400 (1960).

30. R. M. Ball, The Babcock & Wilcox Company, personal communication.

31. "Maritime Reactor Program Annual Progress Report for Period Ending November 30, 1961," ORNL-3238, p. 60.

32. Memorandum, J. A. Bast et al., to E. E. Gross, "Comparison of Zircaloy and Stainless Steel as Structural Materials in the Core of the N.S. SAVANNAH," EPS-X-428 (November 9, 1959).

33. O. J. Marlowe and P. A. Ombrellaro, "CANDLE, A One-Dimensional Few-Group Depletion Code for the IBM-704," WAPD-TM-53 (May 1957).

34. E. A. Nephew, "Thermal and Resonance Absorption Cross Sections of U-233, U-235, and Pu-239 Fission Products," ORNL-2869 (January 18, 1960).

35. "Maritime Reactor Program Annual Progress Report for Period Ending November 30, 1961," ORNL-3238, pp. 73–77.

APPENDICES

Appendix 1. Core Material Compositions

Core I UO_2 (Based on vendor's analysis)

Density = 10.142 g/cm^3

Inner-pass enrichment = 4.19 wt %

Outer-pass enrichment = 4.60 wt % (assumed)

Stainless Steel Tubing (Based on vendor's analysis)

Density = 7.93 g/cm^3 (assumed)

Composition:

Element	Content (wt %)
C	0.054
Mn	1.69
S	0.012
P	0.016
Si	0.56
Cr	18.26
Ni	10.01
Fe	69.298
Co	0.04
Cu	0.05
Mo	0.01

Stainless Steel Fuel-Element Containers (Based on vendor's analysis)

Density = 7.93 g/cm^3 (assumed)

Composition:

Element	Content (wt %)
C	0.041
Mn	1.67
S	0.011
P	0.018
Si	0.32
Cr	18.75
Ni	8.90
Fe	70.281
Co	0.009

Boron-Stainless Steel (Based on vendor's analysis)

Density = 7.93 g/cm^3 (assumed)

Composition:

Element	Content (wt %)
C	0.02
Mn	1.96
S	0.010
P	0.005
Si	0.65
Cr	19.06
Ni	16.23
Fe	60.313
Co	0.012
Cu	0.02
Mo	0.01
B (92 wt % B^{10})	1.71

Zircaloy-2 Followers and Fuel-Element Containers (From Reactor Handbook*)

Density = 6.55 g/cm^3

Composition:

Element	Content (wt %)
Zr	98.289
Sn	1.45
Fe	0.115
Cr	0.09
Ni	0.05
N	0.006

Alumina Filler (Assumed values)

Density = 3.97 g/cm^3

Composition:

Element	Content (wt %)
O	47.1
Al	52.9

*C. R. Tipton, Jr., "Materials," Reactor Handbook, Vol. I, p. 709, Interscience Publishers, Inc., 1960.

Appendix 2

Table 1. Multigroup Transport Cross-Section Data

Group No.	Lethargy Limits	Group Width, Δu	$3\sigma_{tr}$ (barns)											
			Hydrogen	Oxygen	B^{10}	Aluminum	Stainless Steel	Zircaloy	Pu^{239}	Pu^{240}	Pu^{241}	U^{235}	U^{238}	Fissium
1	0–0.5	0.5	1.157	3.3733	11.2106	4.7735	8.5460	18.404	28.8	28.8	28.8	19.3369	8.6157	10.0
2	0.5–1.0	0.5	1.699	3.8813	11.2106	4.4025	8.8675	18.404	28.8	28.8	28.8	20.7573	9.8164	10.0
3	1.0–1.5	0.5	2.306	2.2042	11.2106	7.1495	8.4470	18.404	28.8	28.8	28.8	21.0337	11.2481	10.0
4	1.5–2.0	0.5	3.127	5.5584	11.2106	9.0670	6.9642	18.404	28.8	28.8	28.8	20.5556	12.6975	10.0
5	2.0–2.5	0.5	4.152	11.0687	11.2106	9.6310	6.9157	18.404	28.8	28.8	28.8	18.0849	14.3107	10.0
6	2.5–3.0	0.5	5.422	9.9187	11.2106	11.3605	7.5567	18.404	28.8	28.8	28.8	18.0220	16.0347	10.0
7	3.0–3.5	0.5	7.014	14.1399	11.2106	8.6760	11.0400	18.404	28.8	28.8	28.8	22.3398	17.8108	10.0
8	3.5–4.0	0.5	8.908	10.6900	11.2106	11.6998	9.3860	18.404	28.8	28.8	28.8	33.3397	20.4808	10.0
9	4.0–7.0	3.0	15.543	10.1661	11.2106	7.6391	14.1914	18.404	28.8	28.8	28.8	37.6115	28.2642	10.0
10	7.0–10.0	3.0	20.000	10.8769	11.2106	4.0058	19.8503	18.404	28.8	28.8	28.8	29.1591	29.2012	10.0
11	10.0–11.4	1.4	20.000	10.9248	11.2106	3.9431	29.6285	18.404	28.8	28.8	28.8	24.5116	27.5796	10.0
12	11.4–12.6	1.2	20.000	10.9248	11.2106	3.9369	32.5625	18.404	28.8	28.8	28.8	23.8360	26.2512	10.0
13	12.6–13.4	0.8	20.000	10.9248	11.2106	3.9287	33.3737	18.404	28.8	28.8	28.8	23.8517	26.0268	10.0
14	13.4–13.8	0.4	20.229	10.9248	11.2106	3.9213	32.9525	18.404	28.8	28.8	28.8	23.8517	26.0268	10.0
15	13.8–14.6	0.8	20.250	10.9248	11.2106	3.9113	32.9302	18.404	28.8	28.8	28.8	23.8517	26.0274	10.0
16	14.6–15.8	1.2	20.431	10.9248	11.2106	3.8858	33.6258	18.404	28.8	28.8	28.8	23.7576	27.3717	10.0
17	15.8–16.2	0.4	20.565	10.9248	11.2106	3.9504	34.4345	18.404	28.8	28.8	28.8	23.7619	27.3094	10.0
18	16.2–16.6	0.4	21.261	10.9248	11.2106	4.2743	32.7250	18.404	28.8	28.8	28.8	23.7806	27.0420	10.0
19	16.6–17.0	0.4	21.951	10.9248	11.2106	4.2482	32.3425	18.404	28.8	28.8	28.8	23.8062	26.6775	10.0
20	17.0–17.4	0.4	22.833	10.9248	11.2106	4.2160	32.3925	18.404	28.8	28.8	28.8	23.8257	26.3982	10.0
21	17.4–17.6	0.2	23.319	10.9248	11.2106	4.1985	32.4000	18.404	28.8	28.8	28.8	23.8329	26.3959	10.0
22	17.6–17.8	0.2	23.474	10.9248	11.2106	4.1893	32.3050	18.404	28.8	28.8	28.8	23.8414	26.0418	10.0
23	17.8–18.0	0.2	23.690	10.9248	11.2106	4.1781	32.3100	18.404	28.8	28.8	28.8	23.8507	26.1730	10.0

Table 2. Multigroup Absorption Cross-Section Data

Group No.	Lethargy Limits	Group Width, Δu	σ_a (barns)												
			Hydrogen	Oxygen	B^{10}	Aluminum	Stainless Steel	Zircaloy	Pu^{239}	Pu^{240}	Pu^{241}	U^{235}	U^{238}[a]	U^{238}[b]	Fissium
1	0–0.5	0.5	0	0.246	0.6177	0.0028	0.0530	0.0057	2.00	2.00	4.0	1.4923	0.7950	0.7950	0.0024
2	0.5–1.0	0.5	0	0.066	0.6177	0.0028	0.0539	0.0073	1.90	1.60	4.0	1.5103	0.5915	0.5915	0.0033
3	1.0–1.5	0.5	0	0	0.7165	0.0028	0.0550	0.0093	2.00	1.65	4.0	1.5217	0.6040	0.6040	0.0040
4	1.5–2.0	0.5	0	0	0.7165	0.0028	0.0564	0.0120	1.95	1.50	9.0	1.5372	0.4852	0.4852	0.0052
5	2.0–2.5	0.5	0	0	0.5559	0.0028	0.0582	0.0154	1.70	1.10	13.0	1.5842	0.1572	0.1572	0.0067
6	2.5–3.0	0.5	0	0	0.9389	0.0028	0.0605	0.0198	1.65	0.80	17.0	1.6602	0.1439	0.1439	0.1228
7	3.0–3.5	0.5	0	0	1.4947	0.0020	0.0635	0.0254	1.65	1.00	22.0	1.7993	0.1633	0.1633	0.1515
8	3.5–4.0	0.5	0	0	1.9271	0.0019	0.0673	0.0326	1.65	1.00	33.0	1.9773	0.1957	0.1957	0.1767
9	4.0–7.0	3.0	0	0	4.1878	0.0064	0.0953	0.0855	3.00	1.00	43.0	3.2220	0.4396	0.4396	0.3564
10	7.0–10.0	3.0	0	0	15.3180	0.0012	0.2633	0.3832	8.20	1.00	65.0	10.0542	0.9540	0.9540	2.0728
11	10.0–11.4	1.4	0	0	41.1240	0.0032	0.0500	1.0710	22.50	2.00	65.0	28.5519	1.6993	1.9181	8.7149
12	11.4–12.6	1.2	0	0	76.8000	0.0063	0.0533	0.0043	62.00	5.00	69.0	51.5628	2.2816	2.5653	17.3203
13	12.6–13.4	0.8	0	0	124.7560	0.0104	0.0804	0.0065	114.00	10.00	139.0	73.3216	3.1887	3.5992	8.3572
14	13.4–13.8	0.4	0	0	167.4980	0.0139	0.1067	0.0090	501.70	22.00	182.0	91.2978	0.8542	0.8542	52.5277
15	13.8–14.6	0.8	0	0	229.2400	0.0188	0.1466	0.0122	110.0	25.00	369.0	87.7241	4.9789	5.6199	118.3537
16	14.6–15.8	1.2	0.0003	0	378.8140	0.0313	0.2432	0.0203	41.70	160.00	91.0	23.3876	0.4004	0.4004	9.6507
17	15.8–16.2	0.4	0.0494	0	557.4550	0.0461	0.3587	0.0299	50.30	20,100.00	43.0	77.6763	0.4213	0.4213	80.4437
18	16.2–16.6	0.4	0.0608	0	682.7920	0.0560	0.4367	0.0364	110.90	800.00	54.0	63.2640	0.5157	0.5157	7.8882
19	16.6–17.0	0.4	0.0735	0	829.6110	0.0687	0.5392	0.0445	369.80	230.00	125.0	91.2695	0.6325	0.6325	9.6347
20	17.0–17.4	0.4	0.0892	0	1009.6970	0.0590	0.6558	0.0544	3343.00	160.00	870.0	192.2160	0.7758	0.7758	11.7678
21	17.4–17.6	0.2	0.0950	0	1109.8450	0.0650	0.7200	0.0631	3448.00	147.00	1890.0	244.4580	0.8600	0.8600	13.6547
22	17.6–17.8	0.2	0.1028	0	1170.3640	0.0682	0.7600	0.0698	1623.00	145.00	1500.0	243.4130	0.9008	0.9008	15.0930
23	17.8–18.0	0.2	0.110	0	1227.4860	0.0720	0.8000	0.0771	1042.00	145.00	1110.0	235.3700	0.9450	0.9450	16.6784

[a]At zero power and room temperature.

[b]At full power.

Table 3. Multigroup Fission Cross-Section Data

Group No.	Lethargy Limits	Group Width, Δu	$\nu\sigma_f$ (barns)			
			Pu^{239}	Pu^{241}	U^{235}	U^{238}
1	0–0.5	0.5	5.80	10.0	3.1801	1.9051
2	0.5–1.0	0.5	3.58	10.0	3.2149	1.4142
3	1.0–1.5	0.5	5.80	10.0	3.2411	1.4142
4	1.5–2.0	0.5	5.66	20.0	3.2717	1.0384
5	2.0–2.5	0.5	8.93	30.0	3.3738	0.0668
6	2.5–3.0	0.5	4.78	40.0	3.5349	0.0019
7	3.0–3.5	0.5	4.78	50.0	3.8292	0
8	3.5–4.0	0.5	4.78	75.0	4.1661	0
9	4.0–7.0	3.0	8.50	100.0	6.1297	0
10	7.0–10.0	3.0	22.60	150.0	16.6772	0
11	10.0–11.4	1.4	56.50	150.0	44.4021	0
12	11.4–12.6	1.2	141.20	160.0	79.4698	0
13	12.6–13.4	0.8	247.20	320.0	106.0394	0
14	13.4–13.8	0.4	776.80	420.0	115.5805	0
15	13.8–14.6	0.8	250.00	850.0	107.4555	0
16	14.6–15.8	1.2	56.50	210.0	38.1666	0
17	15.8–16.2	0.4	103.60	100.0	158.4010	0
18	16.2–16.6	0.4	186.0	124.0	138.4789	0
19	16.6–17.0	0.4	565.00	260.0	196.1515	0
20	17.0–17.4	0.4	509.40	2234.0	378.2314	0
21	17.4–17.6	0.2	5265.00	4600.0	473.3222	0
22	17.6–17.8	0.2	2540.00	3400.0	472.8955	0
23	17.8–18.0	0.2	1722.00	2402.0	460.5297	0

ORNL-3261

Reactor Technology
TID-4500 (17th ed.)

Internal Distribution

1. L. G. Alexander
2. F. S. Alsmiller
3. T. D. Anderson
4. V. E. Anderson (K-25)
5. S. E. Beall
6. M. Bender
7. F. Binford
8. E. P. Blizard
9. A. L. Boch
10. R. B. Briggs
11. A. D. Callihan
12. R. S. Carlsmith
13. R. D. Cheverton
14. H. C. Claiborne
15. T. E. Cole
16-17. B. W. Colston
18. J. A. Conlin, Jr.
19. J. G. Delene
20. W. K. Ergen
21. A. P. Fraas
22-26. E. E. Gross
27. P. N. Haubenreich
28. V. O. Haynes
29. D. K. Holmes
30. W. H. Jordan
31. S. I. Kaplan
32. P. R. Kasten
33. W. E. Kinney
34. O. H. Klepper
35. R. B. Korsmeyer
36. J. A. Lane
37. C. E. Larson (K-25)
38. R. S. Livingston
39. T. S. Lundy
40. R. N. Lyon
41. H. G. MacPherson
42. F. C. Maienschein
43. W. D. Manly
44. E. R. Mann
45. J. H. Marable
46. B. F. Maskewitz (K-25)
47. H. C. McCurdy
48. J. T. Mihalczo
49. J. W. Miller (K-25)
50. F. H. Neill
51. L. Nelson
52. E. A. Nephew
53. C. W. Nestor, Jr.
54. A. M. Perry
55. P. H. Pitkanen
56. C. A. Preskitt
57. M. W. Rosenthal
58. T. H. Row
59. A. W. Savolainen
60. L. D. Schaffer
61. E. G. Silver
62. J. A. Swartout
63. W. C. Thurber
64. M. L. Tobias
65. F. C. VonderLage
66. D. R. Vondy
67. D. W. Vroom
68. A. M. Weinberg
69. C. L. Whitmarsh, Jr.
70-71. M. L. Winton
72-75. ORNL-Y-12 Technical Library
Document Reference Section
76-78. Central Research Library
79-100. Laboratory Records Department
101. Laboratory Records Department, R. C.

External Distribution

102. Ira Adler, New York Operations Office, AEC
103. Russ Aven, University of Mississippi

104. D. S. Beard, San Francisco Operations Office, AEC
105. Manson Benedict, Massachusetts Institute of Technology
106. R. F. Benenati, Brooklyn Polytechnic Institute
107. R. A. Charpie, UCC Research Administration, New York, N. Y.
108-109. W. R. Congdon, The Babcock & Wilcox Company, Atomic Energy Division
110. C. M. Copenhaver, MITRE Corporation, Bedford, Mass.
111. J. C. Ebersole, Tennessee Valley Authority
112. P. P. Eddy, General Electric Company, Atomic Equipment Department, San Jose, California
113. D. F. Fieno, National Aeronautics and Space Administration, Cleveland, Ohio
114-115. W. C. Gribble, Division of Reactor Development (Army Reactors), AEC, Washington
116-117. K. Kaschau, Alco Products, Inc.
118. Douglas C. MacMillan, George G. Sharp, Inc., New York
119-120. M. M. Mann, New York Shipbuilding Corporation, Camden, New Jersey
121-125. R. O. Mehann, States Marine Lines, Inc.
126-127. L. J. Meisenheimer, Engineer Research and Development Laboratories, Fort Belvoir, Virginia
128. R. L. Murray, North Carolina State University
129-130. J. F. O'Brien, The Martin-Marietta Company, Nuclear Division
131-133. R. T. Schomer, The Babcock & Wilcox Company, Atomic Energy Division, Lynchburg, Virginia
134. D. H. Shaftman, Argonne National Laboratory
135. W. C. Stamm, Ebasco Services, Inc., New York
136-145. E. K. Sullivan, Division of Reactor Development (Maritime Reactors), AEC, Washington
146. B. W. Winchell, Todd Shipyards Corporation, Nuclear Division
147. Research and Development Division, AEC, ORO
148-149. Reactor Division, AEC, ORO
150-750. Given distribution as shown in TID-4500 (17th ed.) under Reactor Technology Category (75 copies – OTS)